7. Česko-slovenská studentská vědecká konference ve fyzice

Fakulta jaderná a fyzikálně inženýrská

České vysoké učení technické v Praze


# Non-identical kaon femtoscopy at STAR experiment

**Jindřich Lidrych**

**Prague, 2016**

# 7. Česko-slovenská studentská vědecká konference ve fyzice

*Category:* Particle and nuclear physics

*Title:* **Non-identical kaon femtoscopy at STAR experiment** [1]

*Author:* Jindřich Lidrych

*Institution:* Faculty of Nuclear Sciences and Physical Engineering
Czech Technical University in Prague

*Abstract:* Experiments with high-energy heavy-ion collisions study properties of nuclear matter and its transition from hadrons to a state of deconfined quarks and gluons called the Quark-gluon plasma. Femtoscopic measurements of two-particle correlations at small relative momenta reveal the space-time characteristics of the system when the particles in the pair are emitted. The correlations result from quantum statistics, final-state Coulomb interactions, and the strong final-state interactions between the emitted particles.

It has been predicted that correlations due to the strong final-state interactions in a system where a narrow resonance is present will be sensitive, in the region of the resonance to the source size and momentum-space correlations. Such a measurement can provide complementary information to the measurements at very low relative momenta. Pair of unlike-sign kaons are ideally suited for such a measurement, since the system contains a narrow $\phi(1020)$ resonance.

This work presents first systematic study of unlike-sign kaon correlation function, including the region of the resonance, using STAR data from Au+Au collisions at $\sqrt{s_{\mathrm{NN}}}$= 200 GeV. The experimental results are compared to theoretical predictions that include the treatment of resonance formation due to final-state interactions.

*Key words:* Correlation femtoscopy, unlike-sign kaon correlation function, STAR experiment, blast-wave model.

[1] The presented work is a part of my diploma thesis.

# Contents

# CHAPTER ONE

# FEMTOSCOPY

Femtoscopy, measurements of two particle correlations at small relative momenta, is a unique tool for measuring the space-time characteristics of the particle emitting source. In this chapter, this technique known as femtoscopy and its application in the region of a narrow resonance will be introduced.

## 1.1 Femtoscopy

Experiments with high-energy heavy-ion collisions study properties of nuclear matter and its transition from hadrons to a state of deconfined quarks and gluons called the Quark-Gluon Plasma (QGP). Femtoscopic measurements of two-particle correlations at small relative momentum reveal information about the space-time characteristics of the system at the moment of particle emission. The correlations are results of quantum statistics and/or final state Coulomb and the strong final state interaction(FSI) between the emitted particles.

This technique was invented in 1960 when Goldhaber and collaborators observed in proton-antiproton annihilations an excess of pairs of identical pions produced at small relative momenta [1]. These observed correlations, as experimenters correctly asserted, came as a result of quantum statistics. Based on this observation the theoretical background of femtoscopy was developed by G. I. Kopylov and M. I. Podgoretsky in the 1970s [2] . Since then the femtoscopic measurements of two-particle correlations at low relative momenta be- came a standard tool for extracting the space-time extents of particle emitting sources. Nowadays femtoscopic studies include identical particles, as well as non-identical interacting particles [3], [4], [5], [6].

The two-particle correlation function in the most general case, as used for non-identical interacting particles, is expressed as

$$CF\left(\boldsymbol{p_1}, \boldsymbol{p_2}\right) = \int \mathrm{d}^3\boldsymbol{r} S\left(\boldsymbol{r}, \boldsymbol{k^*}\right) \left|\psi_{1,2}\left(\boldsymbol{r}, \boldsymbol{k^*}\right)\right|^2, \tag{1.1}$$

where $S\left(\boldsymbol{r}, \boldsymbol{k}\right)$ is source function describing emission of two particles at a relative distance $\boldsymbol{r}$ with a relative momentum $\boldsymbol{q} = \boldsymbol{p_1} - \boldsymbol{p_2} = \boldsymbol{2k^*}$. The interaction of these particle is encoded into two-particle wave function $\psi_{1,2}\left(\boldsymbol{r}, \boldsymbol{k^*}\right)$.

In case of identical non-interacting particles, the correlation function is a Fourier transformation of the relative source function, into which the time information is convoluted, defined as

$$CF\left(\boldsymbol{P}, \boldsymbol{q}\right) = 1 \pm \int \mathrm{d}^3\boldsymbol{r} \cos\left(\boldsymbol{q} \cdot \boldsymbol{r}\right) S\left(\boldsymbol{r}, \boldsymbol{k^*}\right), \tag{1.2}$$

where $P$ is the average pair momentum. The deconvolution of the t and $\boldsymbol{r}$ can only be done by employing a model describing four-dimensional particle emission. Hence, the experimental measurements of the correlation function goes hand in hand with model treatment of space-time evolution of the considered system.

Experimentally, the correlation function is constructed as a ratio of the measured two-particle inclusive spectra to the single-particle inclusive spectra [7]. Mathematically, this definition can be

written as

$$CF\left(\boldsymbol{p_1}, \boldsymbol{p_2}\right) = \frac{\mathrm{d}N^{12}/\left(\mathrm{d}^3p_1\mathrm{d}^3p_2\right)}{\left(\mathrm{d}N^1/\mathrm{d}^3p_1\right)\left(\mathrm{d}N^2/\mathrm{d}^3p_2\right)}. \tag{1.3}$$

The simplest correlation function is constructed only in one dimension as a function of $q_{inv}$ which is defined

$$q_{inv} = \sqrt{(E_1 - E_2)^2 - (\boldsymbol{p_1} - \boldsymbol{p_2})^2}. \tag{1.4}$$

Then the most common parametrization of the source is via parameter $R_{inv}$ and the one-dimensional correlation function can be written as

$$CF(q_{inv}, \boldsymbol{K}) = 1 + \lambda\left(\boldsymbol{K}\right)\exp\left(-q_{inv}^2 R_{inv}^2(\boldsymbol{K})\right), \tag{1.5}$$

where $\lambda$ is the lambda parameter and $R_{inv}$ is the Gassian source radius. Disadvantage of such a parametrization is the fact that all spacial and temporal information are convulated into $R_{inv}$. On the other hand for low-statistics measurements this can be the only way how to extract space-time extents.

Three-dimensional correlation function in LCMS is often parametrized by

$$CF(\boldsymbol{q}, \boldsymbol{K}) = 1 + \lambda(\boldsymbol{K})\exp\left(-R_o^2(\boldsymbol{K})q_o^2 - R_s^2(\boldsymbol{K})q_s^2 - R_l^2(\boldsymbol{K})q_l^2\right), \tag{1.6}$$

where the interpretaion of the HBT radii is following [8]:

$$\begin{aligned} R_o^2(\boldsymbol{K}) &= \left\langle \left(\widetilde{x} - \beta_T\widetilde{t}\right)^2 \right\rangle \\ R_s^2(\boldsymbol{K}) &= \left\langle \widetilde{y}^2 \right\rangle \\ R_l^2(\boldsymbol{K}) &= \left\langle \left(\widetilde{z} - \beta_l\widetilde{t}\right)^2 \right\rangle. \end{aligned} \tag{1.7}$$

Here, $\beta_l$ and $\beta_T$ are the components of the pair velocity. The symbol $\widetilde{x}$ denotes the $\langle\Delta x\rangle$ and $\langle\rangle$ denotes an average. An important observation resulting from this parametrization, which was extensively experimentally studied, is that the ratio of $R_o^2/R_s^2$ is sensitive to the lifetime $\beta_T$ of the measured source. The lifetime is also often studied via a difference [8]

$$R_{\mathrm{diff}}^2 = R_o^2 - R_s^2 = \beta_T^2\left\langle\widetilde{t}^2\right\rangle - 2\beta_T\left\langle\widetilde{x}\widetilde{t}\right\rangle + \left(\left\langle\widetilde{x}^2\right\rangle - \left\langle\widetilde{y}^2\right\rangle\right), \tag{1.8}$$

where the first term representing the lifetime of the source is dominant [9].

## 1.2 Hydrodynamics and femtoscopy

The measured HBT radii, as it was mentioned in the previous subsection, non-trivially mix spatial and temporal information on the studied source. In addition, the correlation function is sensitive to the relative source function $S\left(\boldsymbol{r}, \boldsymbol{k^*}\right)$ depending on the relative distance of two measured particles $\boldsymbol{r}$. If there exists a correlation between emission points and particle momenta then it is important to understand that the measured radii can not be simply identified as the size of the whole system. The two-particle correlations provide information about the region of the source from which pair of particles with given relative momentum can be emitted. This region is called the homogeneity region and its size is the homogeneity length.

The sizes of the homogeneity regions are influenced by the expansion and space-time evolution of the measured source. As a results of the collective flow, there is the correlation of the total pair momentum and position of the emission, noted as x-p correlations. Therefore HBT radii, the homogeneity lengths, depend on the pair momentum and carry information about the dynamical properties of the source. The dependence of the HBT radii on the pair momentum is illustrated in Figure 1.1 showing homogeneity regions for different magnitudes of pair momenta.

For this reason, to obtain complete insight into space-time evolution of studied source, it is necessary to compare experimental results to models of the heavy-ion collisions which are able to produce the particles with space-time coordinates at the moment of their freeze-out. Hydrodynamical calculations are able to satisfactorily describe the evolution of the created system during heavy-ion collisions.

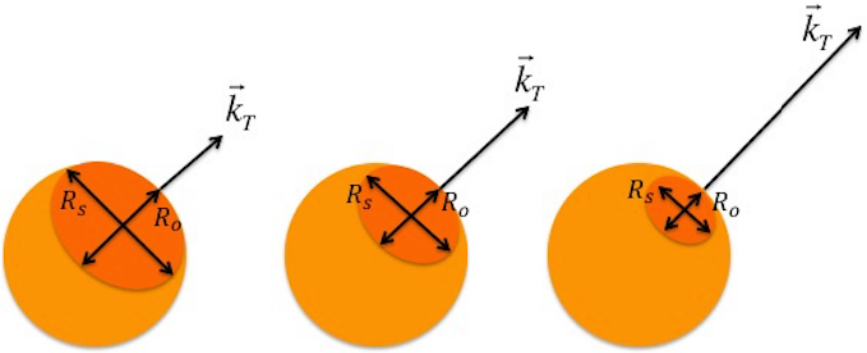


**Figure 1.1:** Homogeneity regions for different pair transverse momenta.

However it is more common and easier to use a family of simplified models which work with hydro-inspired parametrization of the particle emitting source. There are many such models. Some of them can be quite sophisticated, including such effect as resonances and particle decays. Example of this model can be a HYDJET++ [10] or THERMINATOR 2 [11]. In this work, the Blast wave model [12] of Retiere and Lisa will be also used.

### 1.2.1 Blast-wave model

One of the most commonly used model in femtoscopy is the blast-wave parametrization [12]. The blast-wave parametrization is based on the hydrodynamic calculations aiming to describe the system at the freeze-out with a minimal set of parameters. This parametrization allows to calculate at the same time bulk properties such as spectra, elliptic flow as well as HBT radii. In contrast with the full hydrodynamics calculations, the blast-wave model is very fast thus it can be effectively used for simultaneous fitting of experimentally measured observable which are connected with the configuration of the bulk of the system.

In this thesis, the blast-wave parametrization [12] developed by Retiere and Lisa will be used. The model employs eight independent parameters to characterize the source. These parameters are $T$, $\rho_0$, $\rho_2$, $R_y$, $R_x$, $a_s$, $\tau_0$ and $\Delta\tau$ and their physical meaning will be given below. As can be seen, the parameterization provides insight into the final configuration of the system, rather than the initial conditions and evolution of the studied system.

The source is parametrized in the Cartesian coordinate system, where the $x-z$ plane is the reaction plane. The model assumes infinite freeze-out configuration in the $z$(beam) direction, while in the transverse $(x-y)$ plane there is elliptical distribution controlled by the radii $R_x$ and $R_y$. The system is divided into the source elements and their spatial weighting is given by

$$\Omega\left(r,\phi_s\right)=\Omega\left(\widetilde{r}\right)=\frac{1}{1+e^{(\widetilde{r}-1)/a_s}}, \tag{1.9}$$

where the normalized elliptical radius is defined as

$$\widetilde{r}\left(r,\phi_s\right)\equiv\sqrt{\frac{\left(r\cos\left(\phi_s\right)\right)^2}{R_x^2}+\frac{\left(r\sin\left(\phi_s\right)\right)^2}{R_y^2}}. \tag{1.10}$$

The $\widetilde{r}$ hence corresponds to a given elliptical sub-shell within the solid volume of the freeze-out distribution. The emission source has a surface diffuseness parametrized by the density profile $a_s$. The box profile of the surface can be realized by setting $a_s=0$, while the Gaussian shape of the density profile is for $a_s=0.3$

The momentum spectrum of emitted particles from the source element at $(x,y,z)$ is given by a fixed temperature $T$ of the thermal kinetic motion at the rest frame of the elements. It is then boosted by a transverse rapidity $\rho\left(x,y\right)$. The boost strength depends on the centrality of the collisions. Authors of the models assumed that for central collision the rapidity profile linearly changes with the normalized

elliptical radius $\widetilde{r}$. Hence in absence of the azimuthal dependence of the flow all source elements on the outer edge of the source would be boosted with the same transverse rapidity $\rho_0$ in the outward direction. To account for azimuthal flow in non-central collisions, the boost strength is connected with the azimuthal angle $\phi_s$. The dependence of the strength of the flow boost and the azimuthal angle $\phi_s$ is realized via a parameter $\rho_2$. Its physical meaning is the strength of the second-order oscillation of the transverse rapidity. Based on these assumptions the resulting flow rapidity is

$$\rho\left(r,\phi_s\right)=\widetilde{r}\left(\rho_0+\rho_2\cos\left(2\phi_b\right)\right), \tag{1.11}$$

where $\phi_b$ is the azimuthal direction of the boost and $\phi_s$ is the spacial azimuthal angle. In particular, this part of the parametrization produces the source anisotropy and therefore its important for understanding the measurements of the elliptic flow and azimuthal sensitive HBT. The $\rho_2>0$ produces the positive elliptic flow and the boost is stronger in the in-plane direction. On the other hand, the positive elliptic flows can be generated when $\rho_2=0$, however in addition $R_y{>}R_x$ is needed.

As it was discussed the source is the longitudinally boost-invariant and the freeze-out occurs with the Gaussian parametrization

$$\frac{dN}{d\tau}\sim\exp\left(-\frac{\left(\tau-\tau_0\right)^2}{2\Delta\tau^2}\right), \tag{1.12}$$

in longitudinal proper time of the source $\tau=\sqrt{t^2+z^2}$. The $\tau_0$ corresponds to a proper average emission time and the emission duration is equal to $\Delta\tau$. Within this model the time dependence of the emission function enters only via Eq. 1.12. In reality one would naturally expects that all other parameters such $R_x$, $R_y$, $\rho$, etc. would also depend on the time. However such time dependence is beyond spirit of this model and for its inclusion a true dynamic model is needed.

In a summary a single particle emission function in the blast-wave model is parametrized as

$$S\left(x,p\right)=S\left(r,\phi_s,\tau,\eta\right)=m_T\cosh\left(\eta-Y\right)\Omega\left(r,\phi_s\right)\mathrm{e}^{\frac{-(\tau-\tau_0)^2}{2\Delta\tau^2}}\sum_{n=1}^{+\infty}\left(\mp1\right)^{n+1}\mathrm{e}^{-np\cdot u/T}, \tag{1.13}$$

where the $Y$ is rapidity and u is the four-velocity. The bulk properties of the studied system like spectra, elliptic flow or HBT radii can be calculated from the single particle emission function. For example it can be mentioned that azimuthally integrated transverse particle spectra is given by

$$\frac{\mathrm{d}N}{p_T\mathrm{d}p_T}=\int\mathrm{d}\phi_p\int\mathrm{d}^4x S\left(x,p\right). \tag{1.14}$$

and the elliptic flow as

$$v_2\left(p_T,m\right)=\frac{\int_0^{2\pi}\mathrm{d}\phi_p\left\{\cos\left(2\phi_p\right)\right\}_{0,0}\left(p\right)}{\int_0^{2\pi}\mathrm{d}\phi_p\left\{1\right\}_{0,0}\left(p\right)}. \tag{1.15}$$

Detailed discussion on how these observables change with different values of the used parameters can be found in [12].

For the purpose of this thesis, the most important are the conclusions from discussion on how the HBT radii depend on parametrization of the source. Therefore they will be discussed in more detail.

As authors have noted, their model is in agreement with previous work [8], which also show that $R_l^2$ carries information about the lifetime of the source and can be parametrized as

$$R_l^2\left(m_T\right)=\tau_0^2\frac{T}{m_T}\times\frac{K_2\left(m_T/T\right)}{K_1\left(m_T/T\right)}, \tag{1.16}$$

where $K_n$ is the $n$-th modified Bessel function. In combination with the spectra providing temperature $T$, this relation can serve to obtain the emission duration of the measured source. Since the $R_s^2$ contains only spacial information and the value of $R_o^2$ is sensitive to the temporal extents of the source, the dynamical properties of the measured system can be described by the ratio of $R_o^2$ to $R_s^2$ as well as the difference $R_o^2$ and $R_s^2$.

Finally, the effect of the flow included in the blast-wave model and the temperature on the homogeneity regions will be discussed. These effects result into a shift between the average freeze-out

space-time point of different particle species as well as different homogeneity lengths for different particle species.

Due to the radial flow the particles' emission points and momenta are correlated so that the particles with higher momenta are emitted more on the outside of the source. This is the effect of the collective expansion. The size of the emission region is controlled by the transverse flow which competes with the thermal motion.

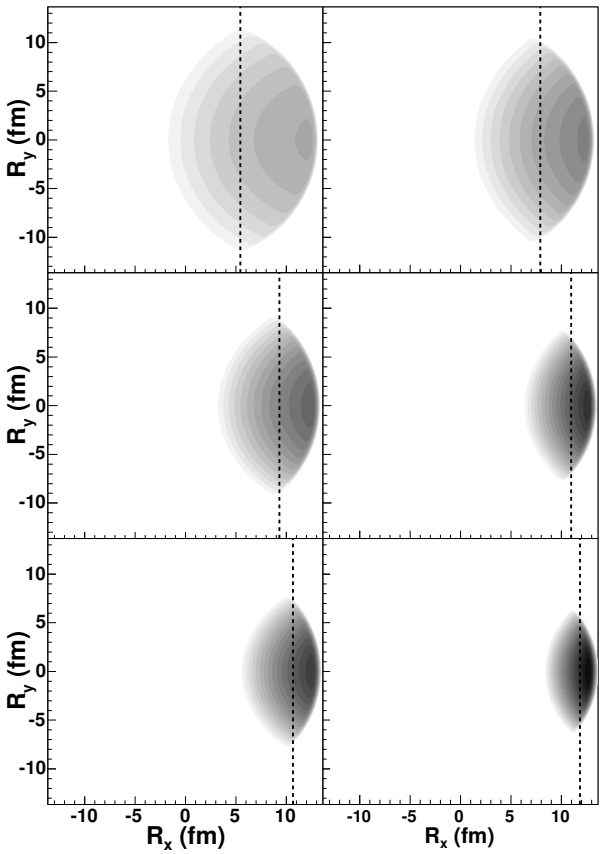


**Figure 1.2:** The homogeneity region and the average emission points for various particle species emitted at the same transverse velocity $\beta_x = 0.907$ on the left-hand side and $\beta_x = 0.974$ on the right-hand side. Top panel is for pion, middle panel for kaons and bottom for proton. Taken from [12].

While the transverse flow decreases the homogeneity length due to the increasing correlation between position and momentum, the thermal motion is superimposed on the flow and increases the size of the homogeneity region by random thermal motion of the emitted particles over a volume of the system. Such phenomenon known as thermal smearing effect makes the particle velocity a sum of the flow velocity $\beta_f$ and the thermal velocity $\beta_t$. Thus in the case of non-identical particles with the same momenta, the average emission points are different.The average emission point of the lighter particle is closer to the center of the system and the homogeneity length corresponds more closely to the size of the studied source. To sum up previous discussion, it can be briefly said that the homogeneity region decreases with the particle $m_T$, while the shift of average emission point increases with the $m_T$. Such dependence is illustrated in Figure 1.2 where the homogeneity regions are shown for different particle species( pions, kaons and protons) emitted with the same velocity. The freeze-out conditions such as temperature, flow profile, freeze-out time and position are the same for all particle species. The dashed lines show the shift of the mean emission position of the homogeneity region.

## 1.3 Collective dynamics and $m_T$ dependence

As was already discussed, the dynamical evolution structure of the source over its lifetime is encoded into its space-time extensions at the freeze-out via space-momentum $(x-p)$ correlations. The expansion and evolution of the measured system is characterized by the collective flow which generates a typical falling off the HBT radii with increasing $m_T$ of the measured pair. Figure 1.3 shows the collection of results on the $m_T$ dependence of the HBT radii from the $\pi^{\pm}-\pi^{\pm}$ correlations from central Au+Au or Pb+Pb collisions. Although the collision energy has changed over the magnitude of two orders, the observed dependence is surprisingly similar for all energies.

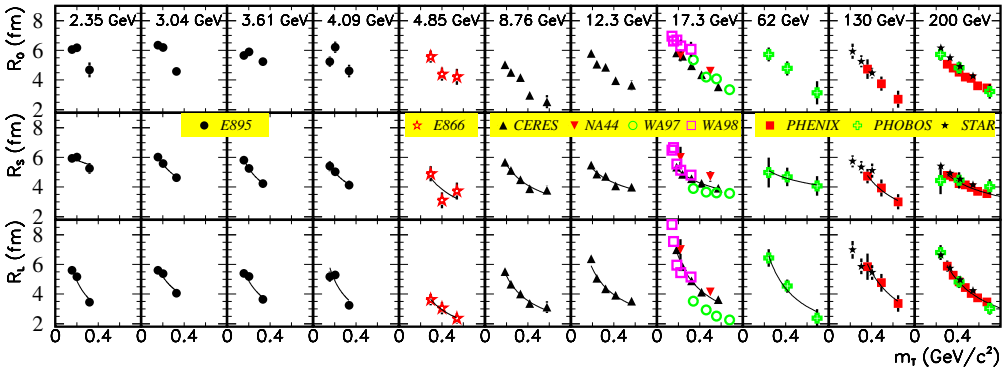


**Figure 1.3:** World data set of $m_T$ dependence of HBT parameters from $\pi-\pi$ femtoscopics measurements. Taken from [7].

As can be seen in Figure 1.4, the $m_T$ scaling is the ubiquitous property of the HBT radii. Figure 1.4 presents results on measured $R_{inv}$ for various particle species with different masses at the same collisions energy. For not so abundant strange particles such as $\Lambda$, only one dimensional correlation functions are accessible. However all of the particle species follow the typical $m_T$ scaling. Such behavior is typical sign of the collection expansion of the system created in heavy-ion collisions.

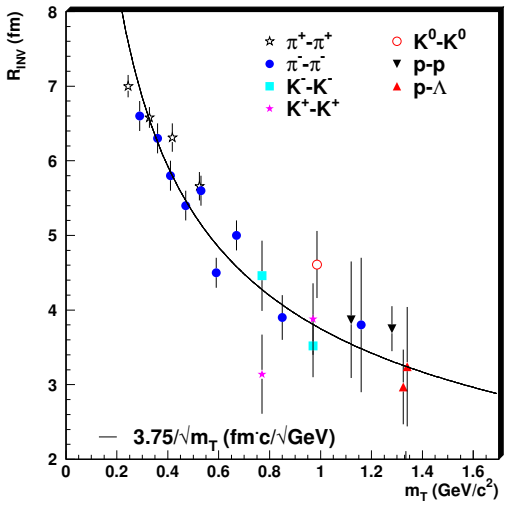


**Figure 1.4:** The universality of $m_T$ dependence of $R_{inv}$ for different particle species. Taken from [13].

## 1.4 Femtoscopy in the region of a narrow resonance

Increasing statistics have already enabled to perform the first femtoscopic analyses with non-identical interacting particles. In addition to $\pi - \pi$ correlations, such studies can provide a new point of view on the created system in the heavy-ion collisions since the various particle species can be sensitive to different effects and different collision stages. However due to lower abundances of these particles, only one dimensional correlation functions have been usually constructed. A solution to these difficulties can be femtoscopy with pairs of particles which contain a narrow, near-threshold, resonance.

It has been predicted that correlations due to the strong final-state interactions in a system where a narrow resonance is present will be sensitive, in the region of the resonance, to the source size and momentum-space correlations [14]. It is expected that the correlation function will be more sensitive in the region of the resonance where the strength of the correlation should change with the source size $r$ as $\sim r^{-3}$ [14] in comparison with measurements at the very low relative momenta, where the correlation function depends on $r^{-2}$ or $r^{-1}$. In addition, these measurements will be statistically advantageous, since the two-particle spectra fall rapidly at low relative momenta. Therefore such a measurement can provide complementary information to the measurements at very low relative momenta.

The sensitivity of the correlation function in the region of the resonance have been already observed at low energy experiments. The left panel of Figure 1.5 shows triton - alpha particle correlation function from measurements which were performed for $^{40}Ar$-induced reactions on $^{197}Au$ at energy $E/A = 60$ MeV [15]. The triton - alpha particle correlation function exhibits several sharp structures resulting from a high lying excited state of $^{7}Li$ which decays into the triton-alpha channel. The theoretical description of such correlation functions can be considerably complicated, nevertheless authors of this analysis [15] made the first estimation. The experimentally constructed deuteron - alpha particle correlation functions, where resonance can be observed, were compared to theoretical correlation function for different source size as is shown in the left panel of Figure 1.5. These functions were predicted by the final-state interaction model and it proved that the correlation function are sensitive to source size in the region of resonance.

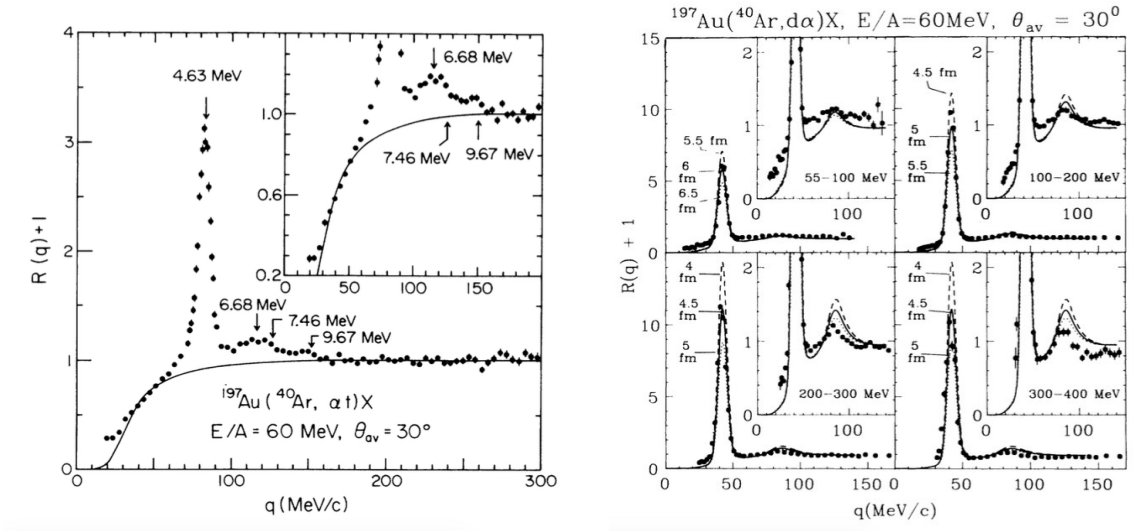


**Figure 1.5:** Left: Triton - alpha particle correlation function from $^{40}Ar$-induced reactions on $^{197}Au$ at energy $E/A = 60$ MeV. The peaks correspond to excited state of $^{7}Li$, which decay into the triton-alpha particle channel. Right: Measured deuteron - alpha particle correlation function are compared to theoretical predictions which takes into account the final-state interaction. Taken from [15].

At high-energy heavy-ion collisions, the similar sharp structure of the correlation function can be also expected. As an example of such function, Figure 1.6 presents the theoretical unlike-sign kaons correlation function calculated by EPOS model. As can be seen, several resonances are visible in the correlation function. In EPOS all resonances, especially the $\phi(1020)$ which is of particular interest for

this work are thermally produced. The difference between the thermal production and the previously mentioned production via the final-state interaction had been widely discussed in [16] and for a case of sudden freeze-out their equivalence had been proved [17].

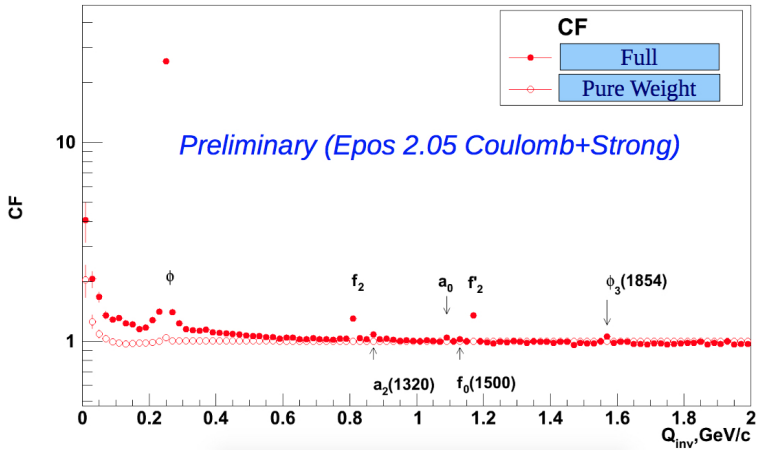


**Figure 1.6:** Theoretical calculated unlike-sign kaons correlation function calculated by the EPOS. Taken from [15].

The femtoscopy in the region of a narrow, near-threshold, resonance brings challenges for the femtoscopics formalism which has been developed for the measurements at low relative momenta. The classical assumptions such as the smoothness approximation and the equal-time approximation will be pushed to the limits. The approach proposed by Lednický [14] extends the femtoscopic formalisms to higher relative momenta between the two emitted particles in a system where the final-state interaction contains a narrow, near-threshold, resonance. The Lednický's FSI model includes the treatment of the $\phi(1020)$ resonance for unlike-sign kaons correlation function and the $\Xi^*(1530)$ resonance for unlike-sign $\pi - \Xi$ correlation. The Lednický model has so far been only to results

The Lednicky model has so far been compared only to results from unlike-sign kaon correlation measured by NA49 collaboration [18] and the preliminary STAR results on $\pi - \Xi$ correlations [19], [20].

In the analysis of $\pi - \Xi$ correlations, the three-dimensional correlation functions have been decomposed in the spherical harmonics. The advantage of such method is the fact that the correlation function [21]

$$C(k^*, \theta, \varphi) = \sqrt{4\pi} \sum_{l=0}^{\infty} \sum_{m=-l}^{l} A_{l,m}(k^*) Y^*_{l,m}(\theta, \varphi), \tag{1.17}$$

is linear combination of the coefficients $A_{l,m}(k^*)$ and the spherical harmonics $Y^*_{l,m}(\theta, \varphi)$. All space-time information about the source is then encoded into the coefficients. While the monopole - $A_{0,0}$ - describes the size of the source, the shift of the mean emission points in out direction is controlled by the dipole $A_{1,1}$.

Although this analysis was statistically challenged, the extracted correlation function [19], [20] shown a strong centrality dependence in the region of the resonance. The preliminary results were compared to the model predictions. Unfortunately none of the used model, FSI, blast-wave neither HYDJET++, did not successfully describe the measured data.

# CHAPTER TWO

# DATA ANALYSIS - CONSTRUCTION OF CORRELATION FUNCTION

The analysis presented in this work is deal with the femtoscopics correlations of unike-sign kaon, including the narrow $\phi(1020)$ resonance. The $\phi(1020)$ resonance with the lifetime of $\sim$ 42 fm/$c$ is characterized by the decay width $\Gamma = 4.3$ MeV and the decay momentum in the rest frame $k^* = 126$ MeV/$c$. A detailed description of the analysis procedure is presented in this chapter. Consequently the data set, event selection, track selection and kaon identification are described. All these cuts lead to construction of two-particle correlation function that is shown in the last section of this chapter.

## 2.1 Data set

The data presented in this work was taken in the year 2011 in Au+Au collisions at $\sqrt{s_{\rm NN}} = 200$ GeV with the minimum bias trigger by the STAR experiment at RHIC. The minimum bias trigger required a coincidence between the East and West ZDC and VPD detectors, respectively. The data are protected against the pile-up. This pile-up occurs when there is such a high rate of collisions that the TPC and other detectors do not have enough time to readout all tracks before the next collision takes place. Therefore it could happen that event would contain a contamination of particles coming from the subsequent events. The detailed information about the used data set in STAR notation is listed below.

- Trigger: vpd-zdc-mb-protected
- Offline Trigger ID: 350003, 350013, 350023, 350033, 350043
- Production: P11id (library: SL11d)
- FileCatalog Command: `trgsetupname=AuAu200_production_2011,filetype=daq_reco_MuDst, filetype=daq_reco_MuDst,filename~st_physics,collisions=AuAu200,sanity=1, available=1,tpx=1,tof=1,storage!=HPSS`
- Number of Events (before event cuts): ~730M

The total number of ~730M events entered the analysis was on which the event cuts were then applied.

## 2.2 Event selection

In order to select events that occurred in the center of the TPC, a cut on the position of the primary vertex along the beam direction ($z$-axis) was applied. The events were required to have $|V_z| < 30$ cm, where $V_z$ is the $z$-coordinate of the primary vertex position measured by the TPC. Such event cut assures that detector acceptance does not change significantly with $V_z$. The primary vertex position

is reconstructed from TPC tracks. Even though, the events are protected against the pile-up which removes large part of the effect, an additional cut on this phenomenon was also applied. This selection criteria uses that fact that the $V_z$ can be calculated from the measured tracks in the TPC as well as by VPD detector that determines $V_z$ of the event on which was triggered. Therefore, the difference between the vertex position measured by the TPC and VPD detectors $\left|V_z - V_z^{VPD}\right|$ were required to be smaller than 5 cm. Both of applied event selection criteria are shown in Figure 2.1.

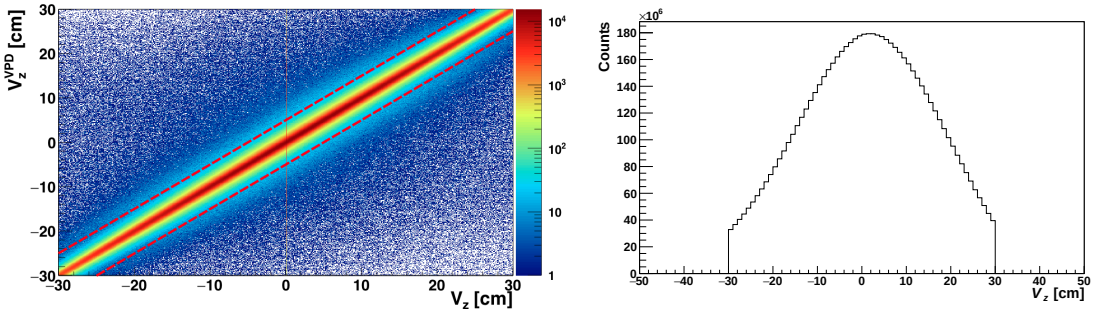


**Figure 2.1:** Left: The distribution of the $z$-coordinate of the primary vertex position measured by the TPC versus the $z$-coordinate of the primary position on which VPD triggered. The red lines represent applied cut. Right: The distribution of the $z$-coordinate of the primary vertex position after applied cut.

### 2.2.1 Centrality definition

There are multiple possible ways how to experimentally define event centrality. The most common method is via the multiplicity of the charged particles. Other observables which are connected to the unobserved impact parameter are the signal from the both of the ZDC detectors and the number of hits recorded by the ToF detector. Correlation between the multiplicity of tracks in TPC and the signal from the ZDC detectors and the ToF Tray multiplicity, respectively is shown in Figure 2.2.

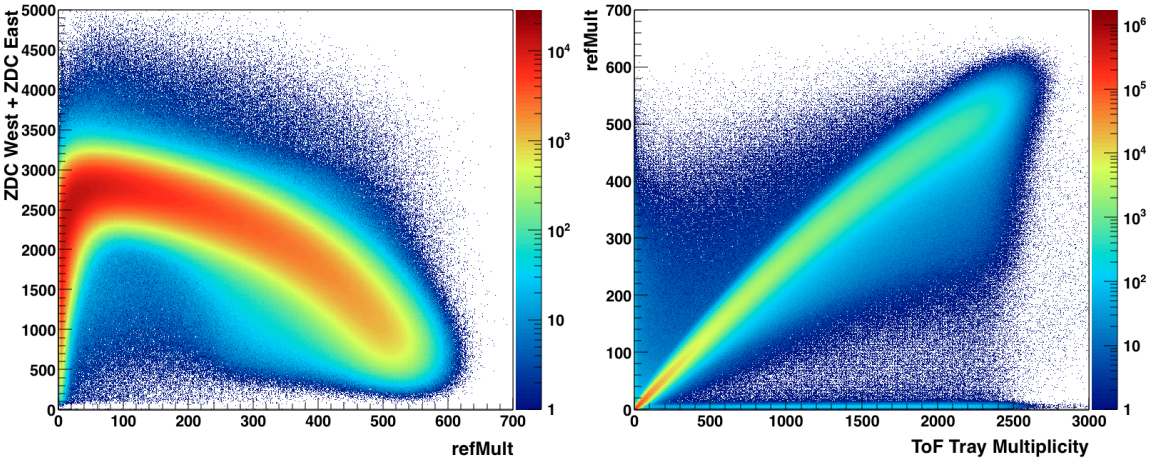


**Figure 2.2:** Left: The correlation between the measured signal by ZDC detectors and TPC multiplicity. Right: The distribution of the reference multiplicity and the ToF tray multiplicity.

In case that the centrality definition is based on multiplicity, the number of charged tracks in TPC, it brings some disadvantages. One of them is a possible dependence of the multiplicity on the primary vertex position. The standard method for removal of this dependency used in the STAR experiment

is via a `StRefMultCorr class`. With the newly obtained corrected multiplicity the centrality can be determined based on the corrected multiplicity. Table 2.1 lists the multiplicity boundaries used in the centrality definition.

| centrality | Multiplicity | centrality | Multiplicity | centrality | Multiplicity |
|---|---|---|---|---|---|
| 0-5% | >466 | 30-35% | >156 | 60-65% | >31 |
| 5-10% | >396 | 35-40% | >125 | 65-70% | >22 |
| 10-15% | >335 | 40-45% | >98 | 70-75% | >15 |
| 15-20% | >281 | 45-50% | >76 | 75-80% | >10 |
| 20-25% | >234 | 50-55% | >58 | | |
| 25-30% | >193 | 55-60% | >43 | | |

**Table 2.1:** Multiplicity boundaries used in the centrality definition.

For the analysis presented in this work, events are divided into 5 bins corresponding to 0-5%, 5-10%, 10-30%, 30-50% and 50-75% centrality. Figure 2.3 shows the multiplicity distribution of the corrected multiplicity divided into these 5 centralities bins. This binning is used for construction of one-dimensional correlation function. Since the first two bins are statistically limited they are later, in construction of the three-dimensional correlation function, merged into one bin.

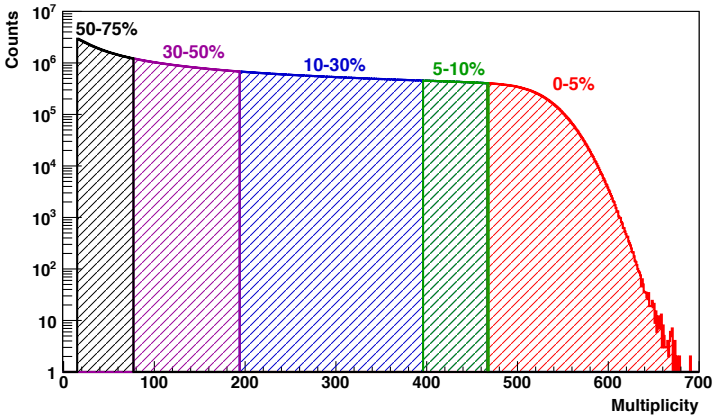


**Figure 2.3:** The corrected multiplicity distribution and corresponding centrality.

In order to remove all non-femtoscopics correlations and to obtain uncorrelated two-particle distribution which is used as the denominator of the experimentally constructed correlation function, mixed pairs from similar events are required. The mixed pairs are constructed in such a way that each particle from one event is mixed with all particles from events belonging to a sub-class of similar events. The division into the subclasses of similar events is done according to the position of the $z$-coordinate of the primary vertex and uncorrected multiplicity. In total, events were divided into 10 bins in the primary vertex position (1bin per 6 cm) and 7 bins in the multiplicity distribution (1 bin per 100 units of multiplicity).

## 2.3 Particle selection

### 2.3.1 Track quality cuts

From the events satisfying the event selection criteria good-quality tracks, particle trajectories, were selected. Only primary tracks with pseudorapidity $|\eta|<1.0$ were accepted. Such cut makes sure that the measured particles fall into the detector acceptance. Then primary tracks were required to have

the distance of the closest approach to the primary vertex smaller than 3 cm. The application of these track quality cuts is shown in Figure 2.4. This way only primary particles were used.

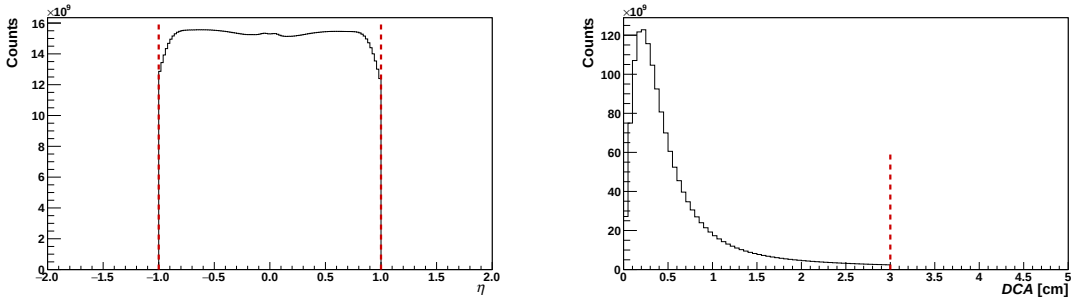


**Figure 2.4:** Left: The distribution of the pseudorapidity of tracks. Right: The distribution of the DCA of tracks. In both cases, the red dotted lines represents applied cuts.

Another *standard* cut which is usually used for the track quality selection is based on the minimal number of reconstructed hits in TPC and the criterion on the ratio of fitted hits to maximum number of hit points. The purpose of these quality cuts is to reduce effects such as track merging or imprecisely reconstructed tracks. Track were required to have minimal 15 fit points in TPC and the ratio of fitted hits to maximal possible hits in TPC was more than 0.52 . There are also criteria which were used by tracking system in order to associate track in TPC with a hit in the ToF.

### 2.3.2 Kaon identification

From the tracks which passed the quality cuts described in the previous section, kaon tracks are selected. In presented analysis, the kaon identification is based on a cut on specific ionization energy loss in the TPC and a cut on mass squared measured by the ToF. These selection criteria are described in more detail below. Since the TPC enables to identify particles with the transverse momentum $p_T$ larger than 0.15 GeV/$c$, in addition a cut on the transverse momenta of the reconstructed tracks was applied. Hence only tracks with $p_T > 0.15$ GeV/$c$ which fulfilled both of the identification cuts were identified as kaons.

#### TPC cut

As was already discussed in the Chapter 2, charged particles are identified via the specific energy loss $\mathrm{d}E/\mathrm{d}x$ in the TPC gas. Due to a finite resolution of the TPC, the measured energy loss deviates from the theoretically expected value calculated using Bichsel function [22]. In case that the measured distribution of the specific energy loss has a Gaussian distribution with the mean value determined by the theoretical value of $\mathrm{d}E/\mathrm{d}x^{theo}$ and with the standard deviation $\sigma_K$, the normalized energy loss for kaon can be defined as

$$n\sigma_K = \ln\left(\frac{\mathrm{d}E/\mathrm{d}x^{meas}}{\mathrm{d}E/\mathrm{d}x^{theo}}\right)/\sigma_{\mathrm{d}E/\mathrm{d}x}, \tag{2.1}$$

where $\mathrm{d}E/\mathrm{d}x^{meas}$ is the measured value of the energy loss. The normalized energy loss is scaled by the resolution $\sigma_{\mathrm{d}E/\mathrm{d}x}$.

In this work, the tracks were required to have $n\sigma_K$ in the range between -3 and 3. As can be seen in Figure 2.5, by applying this cut the hadron contamination can be eliminated up to momentum $p$ $< \sim$0.55 GeV/$c$. However there is a significant presence of the pions at negative $n\sigma_K$ and protons at positive $n\sigma_K$ for higher momenta. The reason for this contamination is the fact that areas of the specific energy loss of pions, kaons and protons overlap for higher momenta. In order to remove the remaining hadron contamination, the ToF cut had to be used as shown in the right panel of Figure 2.5

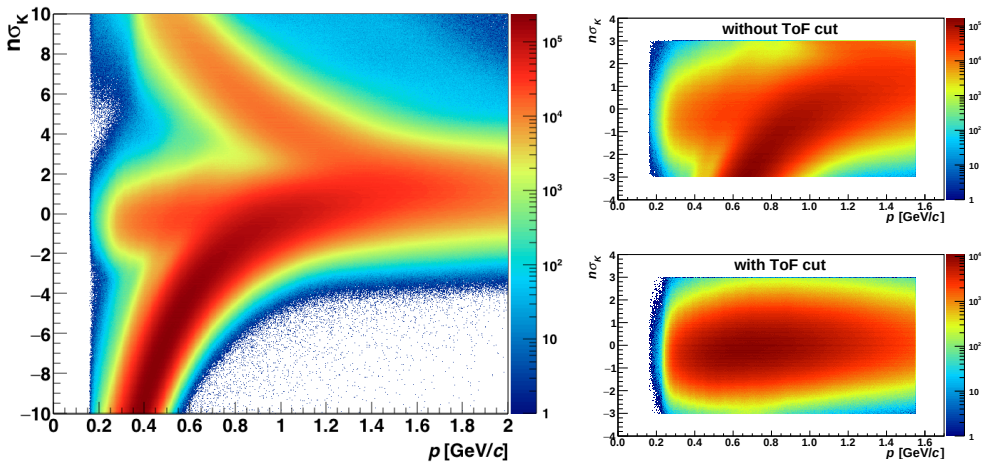


**Figure 2.5:** Left: The distribution of the $n\sigma_K$ versus momentum $p$ of tracks in TPC. Right, Top: The distribution of $n\sigma_K$ versus momentum $p$ without ToF cut. Right, Botton: The distribution of $n\sigma_K$ versus momentum $p$ with ToF cut.

### ToF cut

The ToF measures the time of flight $\beta$. When this information is combined with the measured momentum in TPC, the particle mass $m$ can be calculated by Eq. **??**. As can be seen in the right panel of Figure 2.5, in comparison with TPC, the ToF enables to separate charged kaons from other hadron up to momentum $\sim 1.55$ GeV/$c$. Therefore tracks were required to have momenta in the range $0.15 < p < 1.55$ GeV/$c$. Since for kaons $m_K^2 = 0.2437$ GeV$^2/c^4$, the last identification cut requires the track to have the mass squared in the range $0.21 < m^2 < 0.28$.

The applied identification selection criteria enable to obtain very pure sample of kaons as is shown in Figure 2.6.

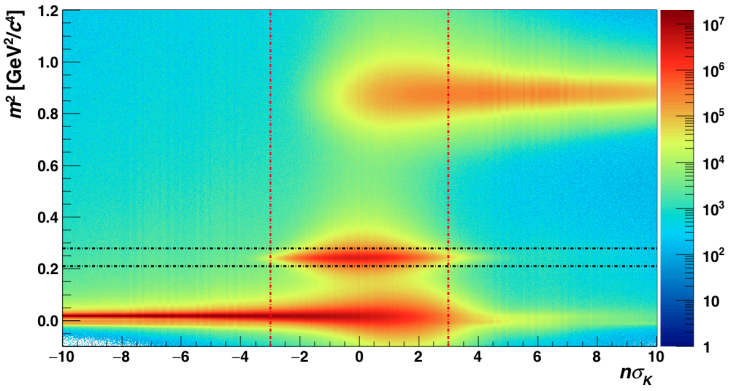


**Figure 2.6:** The distribution of mass square of particle vs $n\sigma_K$. Red lines represent $n\sigma_K$ cut and black lines represent cut on particle mass.

## 2.4 Pair cuts

Despite very clean kaon sample the two particle distribution is affected by detector defects arising from the tracking reconstruction imperfections. The influence of these imperfections exhibits at the

low relative momentum $q_{inv}$, where the measured correlation function is the most sensitive to space-time extents of the source. These effects are track splitting and track merging. In the following two subsections, the cuts which eliminate these effects will be described and tested.

### 2.4.1 Track splitting

The case, when track from single particle is reconstructed as two very close tracks, is called the track splitting [3]. The measured tracks then have very similar momenta, hence their relative momentum $q_{inv}$ is small. Therefore the track splitting causes an enhancement of pairs at low relative momentum $q_{inv}$. In order to remove these split tracks the locations of the hits for each track in the pair in the pad-rows of the TPC were studied. It was performed via the so-called "Splitting level" (SL) calculated as

$$SL = \frac{\sum_i S_i}{NHits_1 + NHits_2}, \tag{2.2}$$

where

$$S_i = \begin{cases} +1 \ldots \text{one track leaves a hit on pad-row} \\ \text{-1} \ldots \text{both tracks leave a hit on pad-row} \\ 0 \ldots \text{neither track leaves a hit on pad-row,} \end{cases} \tag{2.3}$$

where $i$ is the pad-row number of the TPC, and $NHits_1$ and $NHits_2$ are the total number of hits associated to each track in the pair. The main principle of the splitting level is shown in Figure 2.7, where the SL is calculated for four possible cases. As can be seen in Figure 2.7, for two clearly distinct tracks the splitting level takes value equal to -0.5. On the other hand, in case of the possibly split track the splitting level is equal to unity.

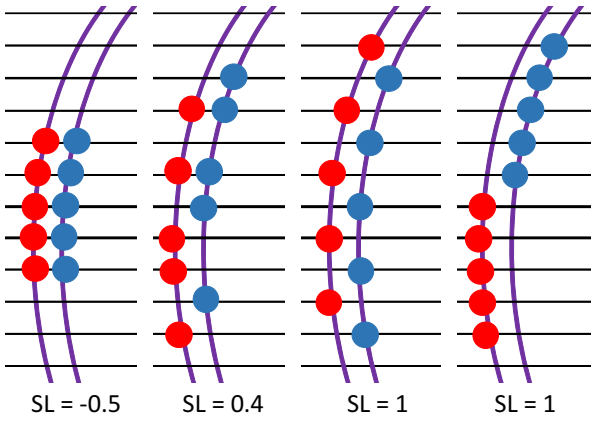


**Figure 2.7:** The description of the anti-splitting cut, which is applied on four possible cases. Red circles are hits assigned to one track, blue circles are assigned to the other.

To remove split tracks, every pair has to fulfilled anti-splitting cut. The value of the anti-splitting cut is determined from the experimentally measured correlation function for different SL. The left panel of Figure 2.8 shows like-sign kaon correlation functions constructed for different values of the SL. As can be seen the effect of the track splitting is not present. The absence of the splitting tracks was also confirmed for unlike-sign kaon correlation functions.

As a cross-check of no influence of the track splitting, the distribution of real pairs versus relative momenta $q_{inv}$ and splittting level were constructed. From the first femtoscopic measurements [3], one would expect to observe the enhancement at low $q_{inv}$ and at higher value of the $SL$. However, The right panel of Figure **??** does not show any enhancement. Similarly, no presence of the track splitting has been recently reported in [23]. One of the possible explanation is the selection criterion on the number of hits in TPC. In the past, track reconstruction was performed with lower number of the hits

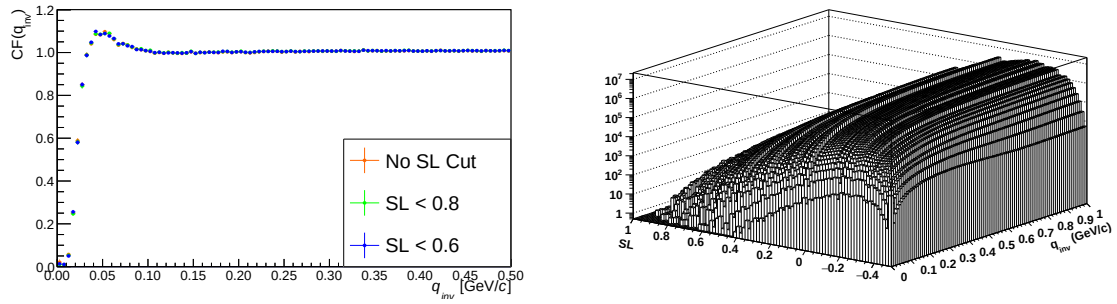


**Figure 2.8:** Left: One-dimensional like-sign kaon correlation function for different values of SL. Right:The distribution of real pairs versus relative momentum $q_{inv}$ and splitting level SL.

in TPC and therefore the track splitting was more frequent. Nevertheless thanks to high available statistics it was possible to apply *standard* SL $< 0.6$ cut to real and mixed pairs and remove whatever possible evidence of the track splitting.

### 2.4.2 Track merging

Besides of track splitting, it can happen that two particles with similar momenta are reconstructed as only one track. It happens when two particles leave hits in the TPC so close to each other that it is beyond the resolution of the read-out pads in the TPC. Two hits are considered merged if the probability of separating them is less than 99% [3]. To determine the maximum fraction of merged hits which eliminates the effect of track merging, the correlation function were constructed for different values of the fraction of the merged hits. Figure 2.9 shows the one-dimensional like-sign correlation functions for different values of the maximum fraction of merged hits. As can be seen, the correlation function is affected by the fraction of merged hits. This effect can be reduces, when the pairs were required to have a fraction of merged hits smaller than 10%.

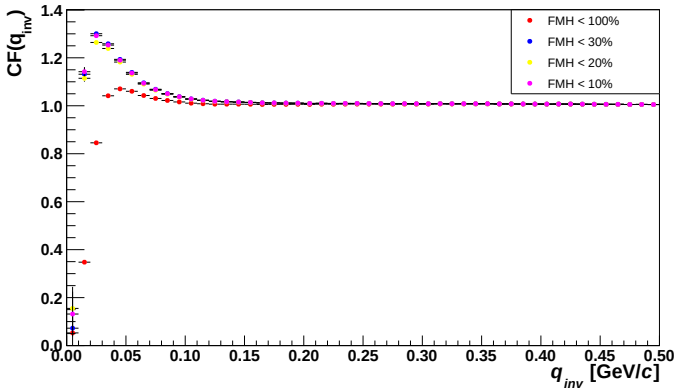


**Figure 2.9:** One-dimensional like-sign correlation function for different values of fraction of merged.

### 2.4.3 $k_T$ cuts

Finally, the last applied cut is on the average pair transverse momentum $k_T$ defined as

$$k_T = \left( \frac{\boldsymbol{p_1} + \boldsymbol{p_2}}{2} \right)_T , \tag{2.4}$$

where $\boldsymbol{p_1}$ and $\boldsymbol{p_2}$ are the momenta of the first and second particle in the given pair, respectively. As was already discussed, homogeneity regions are expected to depend on the pair transverse momentum. Hence such cut enables to change the size of the measured volume at the constant centrality and temperature of the system. The average transverse momentum can be rewritten in the term of the transverse mass of the pair as

$$m_T = \sqrt{k_T^2 + m_0^2}, \tag{2.5}$$

where $m_0$ is the particle's mass. This relation is suitable for study of the $m_T$ dependence of the measured HBT radii which reflects the dynamics of the systems.

In our analysis, the pairs were required to have the average transverse momenta in the range from 0.05 GeV/$c$ to 1.25 GeV/$c$. This range was consequently divided into four bins: 0.05-0.35, 0.35-0.65, 0.65-0.95 and 0.95-1.25 GeV/$c$. Figure 2.10 shows the $k_T$ distribution of real like-sign pairs.

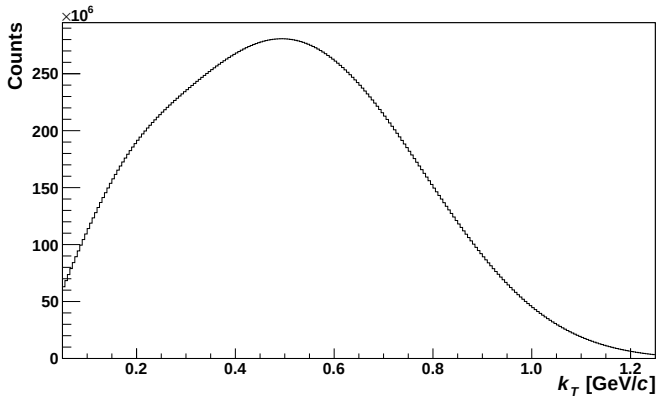


**Figure 2.10:** The distribution of real pair transverse momentum.

## 2.5 Raw one-dimensional correlation functions

Finally, the correlation function $CF\,(q_{inv})$ can be constructed as a ratio of the correlated two-particle distribution from the same event, $N_{same}\,(q_{inv})$ and the uncorrelated two-particle distribution from mixed events, $N_{mixed}\,(q_{inv})$:

$$CF\,(q_{inv}) = \frac{N_{same}\,(q_{inv})}{N_{mixed}\,(q_{inv})} = \frac{real\,pairs}{mixed\,pairs}. \tag{2.6}$$

Figure 2.11 presents results on the unlike-sign kaons correlation function from Au+Au collisions at $\sqrt{s_{\rm NN}} = 200$ GeV. The left panel of Figure 2.11 presents unlike-sign correlations for 4 $k_T$ bins and centrality 30-50%. Centrality dependence of unlike-sign correlation functions, which are integrated over $k_T$ is shown in the right panel of Figure 2.11. While at the low $q_{inv}$ the attractive Coulomb interaction and strong interaction in s-wave can be observed, in the region of $q_{inv} \sim 0.25$ GeV/$c$ the strong interaction in p-wave via $\phi(1020)$ resonance in FSI is present.

As can be seen, the correlation function is sensitive to the source size. In particular, a strong dependence on collisions centrality and on the pair $k_T$ is observed in the resonance region. The height of the $\phi$ peak decreases significantly with the centrality as well as with $k_T$.

Similarly also the like-sign correlation functions were constructed, separately for positively and negatively charged pairs of kaons. The like-sign kaon correlation functions are also sensitive to the space-time extents as shown Figure 2.12. At the low $q_{inv}$, the repulsive Coulomb interaction which competes with Bose-Einstein statistics can be observed. However the region of the low $q_{inv}$ is strongly effected by the statistical uncertainties resulting from the rapidly falling two-particle spectra at low relative momenta.

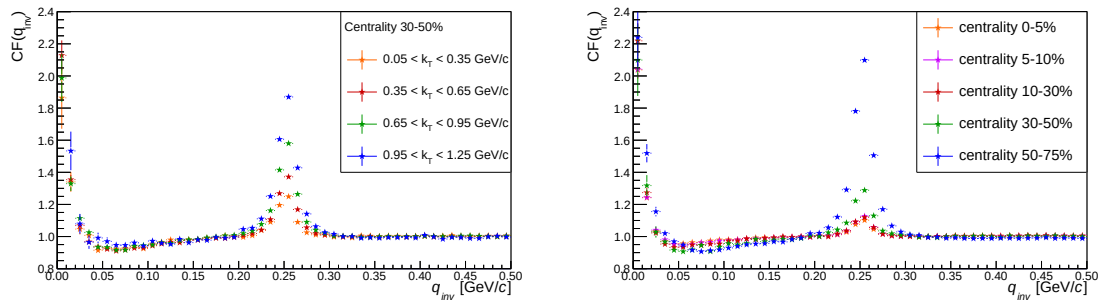


**Figure 2.11:** Top: One dimensional unlike-sign correlation functions for centrality 10-30% and for 4 $k_T$ bins. Bottom: One dimensional unlike-sign correlation functions for 5 centralities.

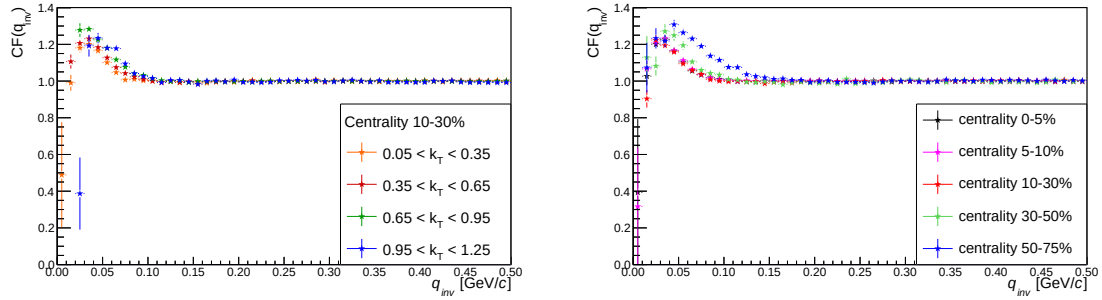


**Figure 2.12:** Top: One dimensional like-sign correlation functions for centrality 10-30% and for 4 $k_T$ bins. Bottom: One dimensional like-sign correlation functions for 5 centralities.

# CHAPTER THREE

# CORRECTIONS OF EXPERIMENTAL CORRELATION FUNCTIONS

Even when very strict selection criteria have been applied, there are additional effect that can alter the strength of the correlation function. They can decrease the strength of the experimental correlation function and affect the extracted HBT radii. One of the main sources of these imperfection is the particle misidentification, when selected the kaon was not actually a kaon. Another effect is related to finite detector momentum resolution.Corrections for both of these effects are introduced below. In this chapter the Coulomb correction required for fitting like-sign correlation functions together with the fitting procedure is also discussed.

## 3.1 Purity correction

Although the single particle cuts were strict and required identification by the ToF in combination with the TPC, it can not be ruled out that some pions or protons could be inaccurately identified as kaons. The misidentified particles then weakened the measured correlation function.Therefore experimental correlation function has to be corrected for misidentification of particles. Since the correlation function depends on the relative momentum $q_{inv}$, the purity correction denoted as PairPurity has to be calculated as a sum of the product of the single particle purities weighted by the probability that two given particles with momenta $\boldsymbol{p_1}$ and $\boldsymbol{p_2}$ form pair with the relative momentum $q_{inv}$. Mathematically it can be expressed as

$$PairPurity\left(q_{inv}\right) = \sum_{\boldsymbol{p_1},\boldsymbol{p_2}} Purity\left(\boldsymbol{p_1}\right) Purity\left(\boldsymbol{p_2}\right) Prob\left(q_{inv}|\boldsymbol{p_1}\boldsymbol{p_2}\right). \tag{3.1}$$

The purity of the particle with momentum $\boldsymbol{p_i}$ is calculated as

$$Purity\left(\boldsymbol{p_i}\right) = Purity_{TPC}\left(\boldsymbol{p_i}\right) Purity_{ToF}\left(\boldsymbol{p_i}\right), \tag{3.2}$$

where $Purity_{TPC}\left(\boldsymbol{p_i}\right)$ is the purity of particles which fulfilled $n\sigma_K$ cut at the given momentum $\boldsymbol{p_i}$, while the purity of particles with momentum $\boldsymbol{p_i}$ which met requirement on their mass squared is referred as $Purity_{ToF}\left(\boldsymbol{p_i}\right)$. The PairPurity has been studied on fraction of the whole sample, ca $\sim$ 150M events.

### 3.1.1 TPC purity

The TPC purity of the particle sample which fulfilled all selection criteria but without applying the $n\sigma_K$ cut was extracted from the $n\sigma_K$ distributions as a function of particle momenta $p$. Figure 3.1 shows example of the two $n\sigma_K$ distributions of positively charged particles with momenta $0.59 < p < 0.61$ GeV/$c$ and $0.99 < p < 1.01$ GeV/$c$ for centrality 10-30%. While for the lower momenta, the three Gaussians distribution are clearly observed, with increasing momenta the Gaussians are merged and finally only one Gaussian remains. The Gaussian centered at zero corresponds to kaons. This

Gaussian is gradually contaminated by the pion Gaussian coming from the negative value of the $n\sigma_K$ and for very high momenta also by the proton Gaussian from the right side. Such behavior is in agreement with presented Figure 2.5 where $n\sigma_K$ as a function of momenta $p$ was shown.

The purity was calculated as the ratio of the kaon Gaussian integrated from -3 to 3 from which the pion's and proton's contributions were subtracted and multi Gaussian also integrated from -3 to 3 expressed as

$$Purity_{TPC} = \frac{\int_{-3}^{3} N_K(\sigma)\,\mathrm{d}\sigma - \int_{-3}^{3} N_\pi(\sigma)\,\mathrm{d}\sigma - \int_{-3}^{3} N_p(\sigma)\,\mathrm{d}\sigma}{\int_{-3}^{3} N_{all}(\sigma)\,\mathrm{d}\sigma}, \tag{3.3}$$

where $N(\sigma)$ is Gaussian distribution. The boundaries of the integral are equal to the range of the applied $n\sigma_K$ cut.

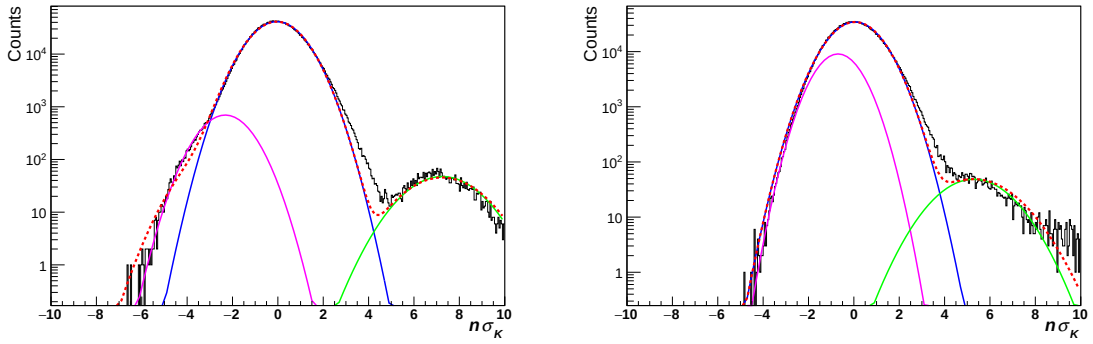


**Figure 3.1:** The distribution of $n\sigma_K$ for $0.59 < p < 0.61$ GeV/$c$ and $0.99 < p < 1.01$ GeV/$c$ for positively charged kaons for centrality 10-30%. Blue line represents kaon Gaussian, magenta line represents pion Gaussian and green line if for proton Gaussian. Their sum is represented by red dotted line.

It is apparent that the fitting becomes complicated with increasing particle momenta $p$ since the Gaussians start to overlap. In order for the fits to convergence, some of the fit parameters their value have to be constrained. There are two possible ways how to limit parameters of the pion Gaussian. The first is based on the theoretical calculation, when the distance between the mean of pion and kaon Gaussian for given momentum is calculated from Bichsel function [22]. However such approach does not take into account detector effects. In our analysis, the identification cuts were changed to select pions and the mean of the pion Gaussian distribution was studied as a function of $n\sigma_K$. This additional study provided information on how to restrict the maximal and minimal values of the mean of the pion Gaussian at the moment when it was overlapped by the kaon Gaussian.

Figure 3.2 shows extracted purity as a function of particle momentum for positively charged kaons for centrality 10-30%. As can be seen, the contaminations of pions and protons is removed by the ToF cut hence the TPC purity is very high, around $\sim 98\%$ and slightly decreases with increasing $p$. Similarly high purity was also observed for all centralities. The same applies for negatively charged kaons.

### 3.1.2 ToF purity

Similar method was employed to extract the purity of the kaon sample for the ToF cut. The ToF purity was extracted from the mass squared distribution. Unlike in previous cases, now the distributions were fitted by Student's t-probability distribution defined as

$$\mathcal{N}\frac{\Gamma\left(\frac{\nu+1}{2}\right)}{\sqrt{\nu\pi}\,\Gamma\left(\frac{\nu}{2}\right)}\left(1+\frac{(x-\mu)^2}{\nu}\right)^{-\frac{\nu+1}{2}}, \tag{3.4}$$

where $\nu$ is the variance, $\mu$ is the mean and $\mathcal{N}$ is the constant. All of these parameters were free parameters of the fit. Figure 3.3 shows the distribution of the mass squared for $0.95 < p < 1.03$

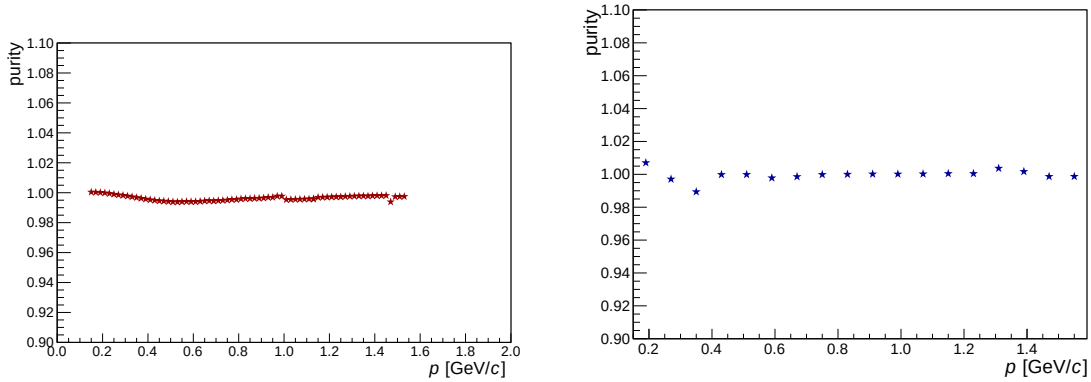


**Figure 3.2:** Left: The TPC purity as a function of momentum $p$. Right: The ToF purity as a function of momentum $p$

GeV/$c$ and $1.43 < p < 1.51$ GeV/$c$ for positively charged kaons for centrality 30-50%. As can be seen in Figure 3.3, now the mean of the distribution is well-defined in contrast to the previous TPC cases. The means should be equal to squared values of pion and kaon masses, respectively. The disadvantage of this procedure is that even after fitting there is some remaining residual background that was fitted by the third-order polynomial functions. In our analysis, it is assumes that the contamination from protons can be neglected.

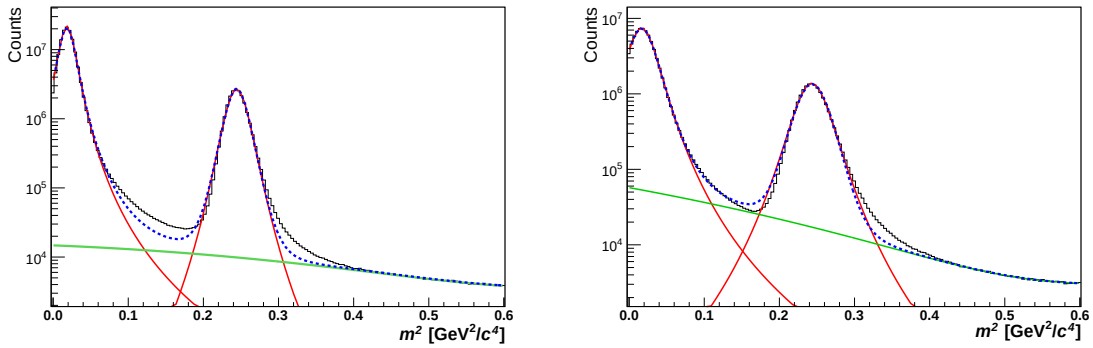


**Figure 3.3:** The distribution of the mass squared of positively charged kaons for $0.95 < p < 1.03$ GeV/$c$ and $1.43 < p < 1.51$ GeV/$c$ for centrality 30-50% measured by ToF. Red lines represent pion and kaon Student's t-probability distributions. Blue line is for Multi-Student's t-probability and the background is represented by the green lines.

The ToF purity as a function of the momentum $p$ is shown in the right panel of Figure 3.2. Similarly as for the TPC purity, also the ToF purity is very high.

### 3.1.3 Probability matrix

Finally the PairPurity is calculated according to Eq. 3.1 where the probability that two given particles with momenta $p_1$ and $p_2$ form pair with the relative momentum $q_{inv}$ is determined by the probability matrix obtained from measured data. The left panel of Figure 3.4 shows probability matrix for positively charged pairs of kaons for centrality 10-30%.

The PairPurity for positively charged kaons for centrality 30-50% is shown in right panel of Figure 3.4. As can be seen, the purity is very high. Similarly high purity was measured for all centralities as well as for negatively charged kaons, even for unlike-sign kaons. Hence the applied correction on raw

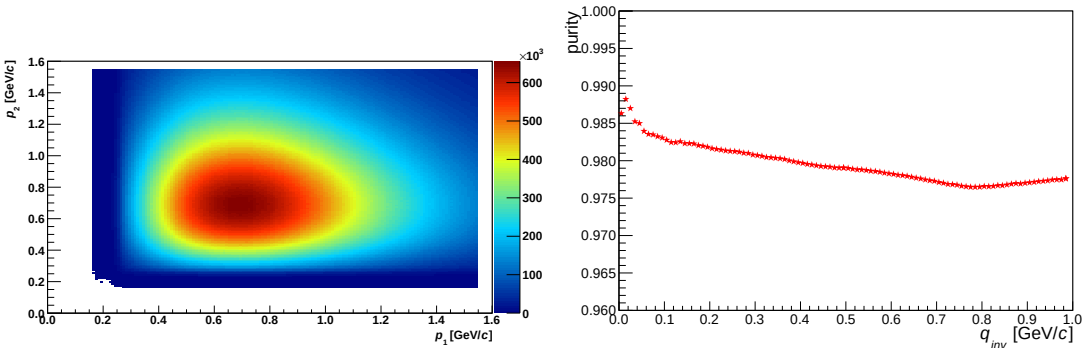


**Figure 3.4:** Left: The probability matrix distribution of two particles with momenta $p_1$ and $p_2$ forming pair with the relative momentum $q_{inv}$. Right: The PairPurity for positively charged kaons for centrality 30-50%.

correlation function $CF^{raw}(q_{inv})$ via relation

$$CF^{corr}(q_{inv}) = \frac{CF^{raw}(q_{inv}) - 1}{PairPurity(q_{inv})} + 1 \tag{3.5}$$

was rather small.

## 3.2 Coulomb correction of like-sign correction function and fitting procedure

In case of the unlike-sign correlation function, there is no analytical parametrization that could be used for fitting. Nevertheless these functions can be fitted numerically. One of the most sophisticated fitting program enabling fitting without the knowledge of the exact form of the correlation function is CorrFit [24] developed by Adam Kisiel. In the presented work, the CorrFit has not been employed so far due to its inherent difficulty. In future it is possible that it will be used.

Instead of unlike-sign correlation function, the like-sign correlation function can be fitted. Hence the source parameters such as the sizes of the source and the $\lambda$ parameter can be obtained so far and used for calculation of the unlike-sign correlation function. The kaons are charged particles, hence the correlation function can not be simply fitted by Eq. 1.5 or Eq. 1.6 because of the dominant Coulomb interaction at the low $q_{inv}$. The Coulomb interaction is repulsive for like-sign kaons and causes a suppression of the correlation function at the low $q_{inv}$.

In presented analysis the Bowler-Sinyukov fitting procedure was used [25]. This method is based on separation of the Coulomb interaction from the Bose-Einstein correlations. Then the one-dimensional correlation function, which is normalized to unity at large $q_{inv}$ is fitted to:

$$CF(q_{inv}) = \left[(1-\lambda) + \lambda K_{Coul}(q_{inv})\left(1 + e^{-q_{inv}^2 R_{inv}^2}\right)\right]\mathcal{N}, \tag{3.6}$$

where $\mathcal{N}$ is the normalization and $K_{Coul}$ is the Coulomb factor defined by Eq. **??**. The free parameters of the fit are $R_{inv}$, $\lambda$ and $\mathcal{N}$. The fit region is for $q_{inv} < 0.4$ GeV/$c$.

The normalization has to be calculated in the region where there is no correlations. Therefore the first estimation of the normalization was calculated in the range from $q_{inv} = 0.6$ GeV/$c$ to $q_{inv} = 1.0$ GeV/$c$. In this region, the measured correlation function is already flat since the Bose-Einstein statistics as well as Coulomb interaction are dominated at the low $q_{inv}$.

In case of the three-dimensional correlation function, the fitting function is expressed as

$$CF(q_o, q_s, q_l) = \left[(1-\lambda) + \lambda K_{Coul}(q_{inv})\left(1 + e^{-q_o^2 R_o^2 - q_s^2 R_s^2 - q_l^2 R_l^2}\right)\right]\mathcal{N}. \tag{3.7}$$

Also here the correlation function is corrected by the Coulomb factor that depends on $q_{inv}$. However, in our cases, due to low statistics, the normalization $\mathcal{N}$ was fixed on the value calculated at the region

$0.3 < q_i < 0.5$ GeV/$c$. Similarly to the fitting of one-dimensional correlation function, the fitting range is from $q_i = 0$ GeV/$c$ to $q_i = 0.4$ GeV/$c$.

In both cases, the best fit is determined on the principle of maximum log-likelihood minimization function [26] defined as

$$\chi^2 = -2\left[A\ln\left(\frac{C\,(A+B)}{A\,(C+1)}\right) + B\ln\left(\frac{A+B}{B\,(C+1)}\right)\right], \tag{3.8}$$

where $C$ is the ratio of the numerator $A$ to denominator $B$. Although no significant difference between the log-likelihood method and the classical $\chi^2$ fitting was observed during fitting one-dimensional correlation function, the implementation of this procedure was motivated by the nonconvergence of the $\chi^2$ method in fitting three-dimensional correlation functions. This procedure is more adequate for lower statistics, where the $\chi^2$ test converges with difficulty. The divergence of the $\chi^2$ is caused by the fact that the ratio of two Poisson distribution is not Poisson distribution itself, especially when taking the ratio of small numbers [7]. The log-likelihood method is described in [26] where the full derivation of the minimization function can be found.

The systematic errors related with the fitting procedure were studied by varying fit range and the normalization region.

The results of fitting, the extracted HBT radii and the $\lambda$ parameters, are intentionally not presented in this section since the correlation functions are still uncorrected on the momentum resolution. However, the procedure providing correction for momentum resolution needs a first estimate of the HBT radii and the $\lambda$ parameters. This procedure will be presented in following section. Only after application of all corrections on experimental correlation functions, the final HBT radii and the $\lambda$ parameters will be extracted and presented.

## 3.3 Momentum resolution correction

Due to the finite particle momentum resolution of the TPC, there is a systematic uncertainty in the determination of $\boldsymbol{q_{inv}}$ which leads to decrease of the strength of the measured correlation function. The effect is stronger in low $q_{inv}$ hence it has significant influence on the extracted radii. Therefore these effects of the momentum resolution have to be corrected.

The magnitude of this effect can be estimated by Monte-Carlo simulations when the simulated particle is embedded into the real event and passed through whole reconstruction process. Such simulation can provide information about the momentum resolution and its influence on the measurable variables.

The components of the real momentum $\boldsymbol{p}$ can be expressed in the term of the measured transverse momentum $p_T$, the azimuthal angle $\varphi$ and the polar angle $\theta$ as

$$\begin{aligned} p_x &= p_T\cos(\varphi) \\ p_y &= p_T\sin(\varphi) \\ p_z &= \frac{p_T}{\tan(\theta)}. \end{aligned} \tag{3.9}$$

However, these components are reconstructed with following deviations:

$$\begin{aligned} \delta p_x &= p_x\frac{\delta p_T}{p_T} - p_y\delta\varphi \\ \delta p_y &= p_y\frac{\delta p_T}{p_T} + p_x\delta\varphi \\ \delta p_z &= p_z\frac{\delta p_T}{p_T} + p_T\frac{\delta\theta}{\sin^2(\theta)}. \end{aligned} \tag{3.10}$$

where the $\frac{\delta p_T}{p_T}$, $\delta\varphi$ and $\delta\theta$ are during the data analysis unknown and have to be extracted from the simulations. Here the kaon embedding for run of 2011 was used. The Monte Carlo simulations contains in total 144 164 positive kaons and 145 383 negative kaons.

Figure 3.5 shows the extracted distribution of the $\frac{\delta p_T}{p_T}$, $\delta\varphi$ and $\delta\theta$ as the function of the $p_T$. These distributions were then parametrized by the Gaussian and its mean and width were studied as the

function of the $p_T$. In Figure 3.6 there are the mean and width of the $\frac{\delta p_T}{p_T}$, $\delta\varphi$ and $\delta\theta$, respectively. The data are fitted with the same functions which were used in [27], [3] and [28]. While the mean of the $\frac{\delta p_T}{p_T}$ is fitted with

$$f\left(p_T\right) = a + bp_T^{\alpha} + cp_T, \tag{3.11}$$

the others are fitted with

$$f\left(p_T\right) = a + bp_T^{\alpha}, \tag{3.12}$$

where $a$, $b$, $c$ and $\alpha$ are the free parameters of the fits. These functions do not have any deeper physical motivation, they just describe well the asymptotic behavior at the low and high $p_T$. It has been shown that the momentum resolution does not depend on the collision centrality and is almost similar for positively and negatively charged kaons. Therefore it was possible to merge both datasets and study the effects of the momentum resolution for all centralities.

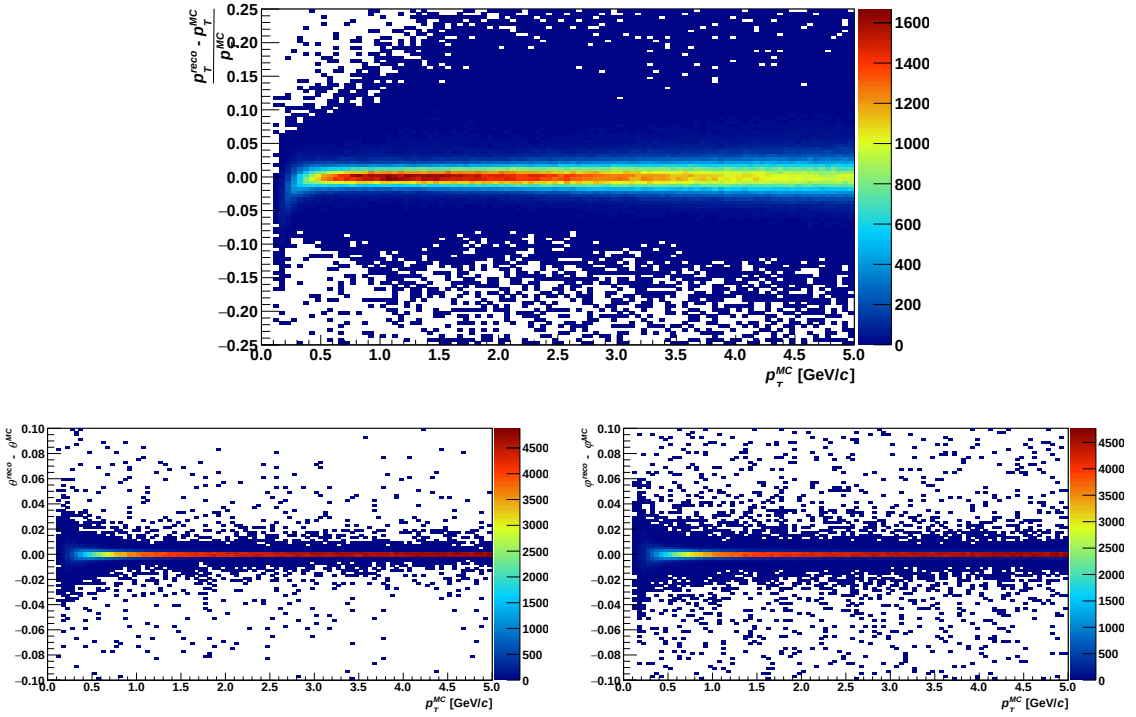


**Figure 3.5:** Monte Carlo simulations for kaons. Top: The distribution of $\frac{\delta p_T}{p_T}$ as a function of $p_T$. Bottom, Left: The distribution of $\delta\theta$ as a function of $p_T$. Bottom, Right: The distribution of $\delta\varphi$ as a function of $p_T$

To estimate the effect of the momentum resolution, two correlation function have to calculated. While the first is the ideal one, the second on is constructed from particles with their momenta randomly smeared. The method how to construct these functions is described below.

First of all, the source was parametrized by a Gaussian in the CMS with a parameter $R_{inv}$. Here the individual $R_{inv}$ were those extracted from fitting like-sign correlation function discussed in the previous section. Hence the distribution of the position for $x$, $y$ and $z$-direction is Gaussian. The momentum distribution of kaons was obtained from analyzed data from different events.Each pair in the numerator in the correction function was weighted according to the following formula

$$weight = (1-\lambda) + \lambda K_{Coul}\left(q_{inv}\right)\left(1 + e^{-q_{inv}^2 R_{inv}^2}\right), \tag{3.13}$$

where the $\lambda$ parameter was the same one as obtained from fitting like-sign correlation function (see Figure 4.2). The second part of the weight factor $K_{Coul}\left(q_{inv}\right)\left(1 + e^{-q_{inv}^2 R_{inv}^2}\right)$ was calculated by the

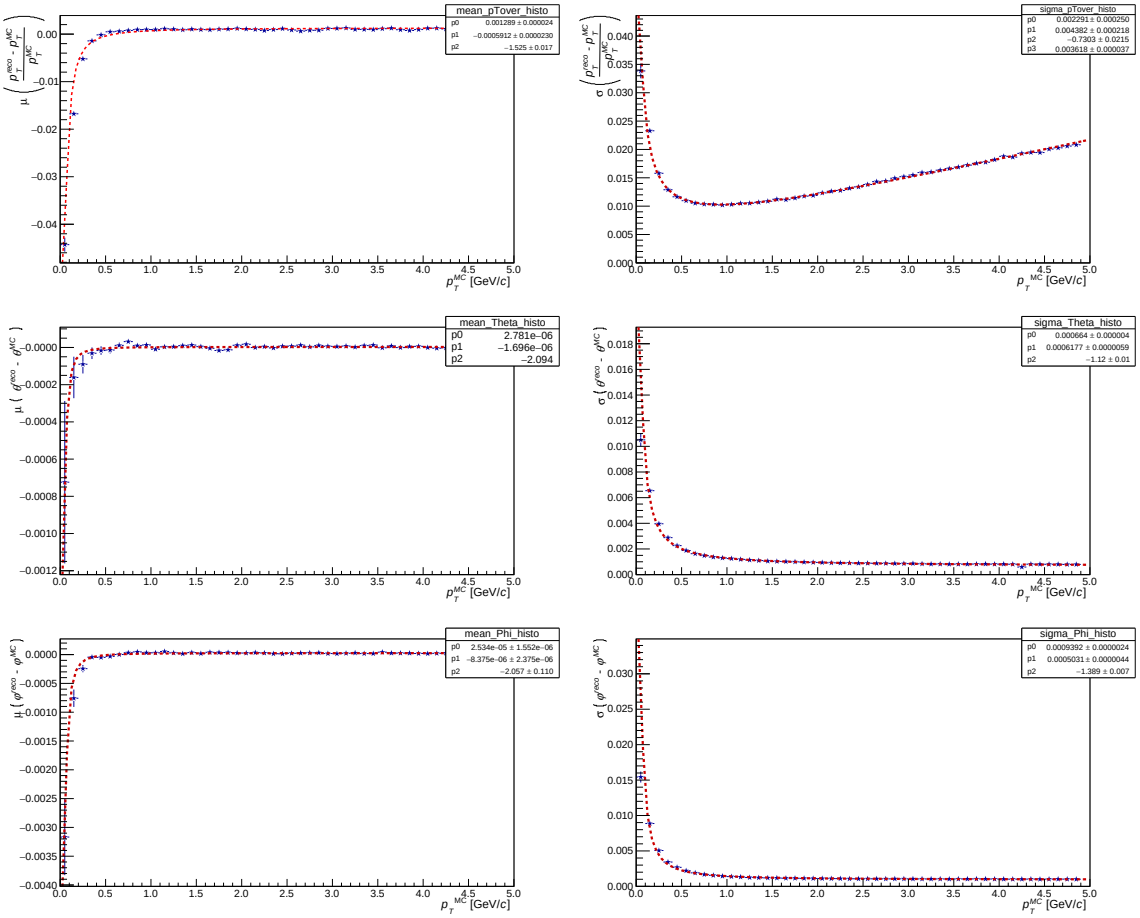


**Figure 3.6:** The $\mu$ and $\sigma$ of the Gaussian distribution of the $\frac{\delta p_T}{p_T}$, $\delta\varphi$ and $\delta\theta$ as a function of the transverse momentum.

Lednický-Lyuoboshitz model. These pairs then formed the numerator of the correlation function. Now the theoretical correlation function can be constructed. In comparison with experimentally measured correlation function, such constructed function is not influenced by any detector effects.

To obtain function that corresponds to the measured one, the momenta of particles had to be smeared according to the extracted momentum resolution (see Figure 3.6). Then the pairs are weighted with the same factor ( Eq. 3.13) which was already used for unsmeared pairs. This procedure causes that the pairs with smeared momenta and the given weight have slightly different $q_{inv}$. This function was denoted as the smeared one and include the effect of momentum resolution. The left panel of Figure 3.7 shows the clean and smeared correlation function constructed by the process discussed above. As can be seen the effect momentum resolution is dominant in the region of the low $q_{inv}$, especially in the region where the Coulomb interaction is dominant. In Figure 3.7 the smeared correlation is also compared to the experimentally measured one. The observed small disparity in the shape of the correlation function can come from using the Bowler-Sinyukov method. The measured function is fitted by Bowler-Sinyukov approximation, while the calculated function was obtained from the exact Lednický-Lyuboshitz analytical model.

To quantify the magnitude of the momentum resolution on the correlation function, the correction factor is constructed as

$$K\left(q_{inv}\right) = \frac{CF^{ideal}\left(q_{inv}\right)}{CF^{smear}\left(q_{inv}\right)} = \frac{\frac{A\left(\boldsymbol{p_1}^{idea}, \boldsymbol{p_2}^{idea}\right)}{B\left(\boldsymbol{p_1}^{idea}, \boldsymbol{p_2}^{idea}\right)}}{\frac{A\left(\boldsymbol{p_1}^{smear}, \boldsymbol{p_2}^{smear}\right)}{B\left(\boldsymbol{p_1}^{smear}, \boldsymbol{p_2}^{smear}\right)}}, \tag{3.14}$$

where the $CF^{clean}$ and $CF^{smear}$ are the ideal and smeared correlation function, respectively. Example of the correction factor for like-sign kaon correlation function for centrality 30-50% and $0.35 < k_T < 0.65$ GeV/$c$ is shown in the right panel of Figure 3.7.

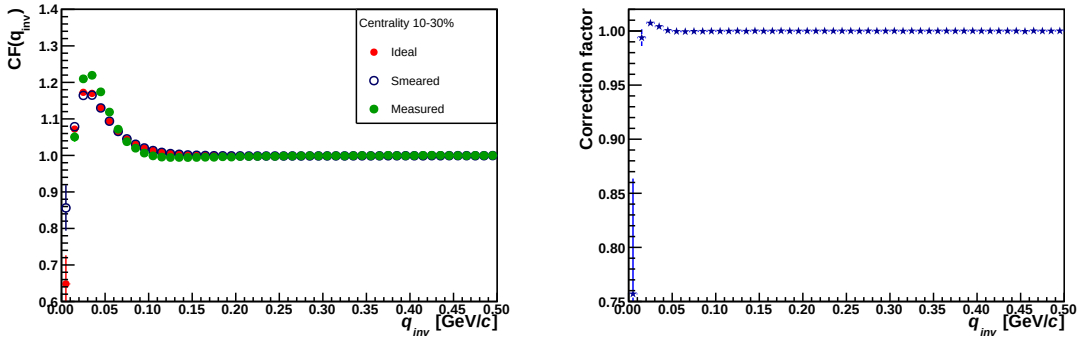


**Figure 3.7:** Left: The smeared correlation function is compared to the clean theoretical function and the experimental correlation function. Right: The correction factor as a function of $q_{inv}$.

In order to remove the effect of the momentum resolution on experimentally measured correlation function $CF^{raw}(q_{inv})$ and to obtain corrected experimental function $CF^{corr}(q_{inv})$, the correction factor is applied as

$$CF^{corr}(q_{inv}) = CF^{raw}(q_{inv})\, K(q_{inv})\,. \tag{3.15}$$

The same correction is also used in the case of the three-dimensional correlation function.

Such corrected correlation functions can be refitted by the same method as was described in the previous section. In our analysis, the effect of this correction is an increase on the HBT radii between 5% and under up to 10% for the highest $k_T$ bin. In case of the largest changes of the HBT radii, this method can be used iteratively until the moment when the difference of newly extracted radii and the ones used for calculation is smaller than a required value. However this iterative method can be significantly time consuming.

One of the possible improvements which will be performed in the future is parametrization the source by the three Gaussian: $R_o$, $R_s$ and $R_l$.

# CHAPTER FOUR

# RESULTS

In the previous two chapters the construction of experimental correlation function and applied corrections were discussed. In this chapter the corrected correlation functions are studied in detail.

In the first part of this chapter the results from like-sign kaon correlation function are presented. The like-sign correlation function is used to extract space-time extents of the source. Using the obtained radii it is possible to compare the unlike-sign kaon correlation functions to Lednický model [14]. This model contains treatment of the $\phi(1020)$ resonance due to the final-state interaction. A detailed study of sensitivity of the unlike-sign kaon correlation functions in the region of the $\phi(1020)$ resonance is presented. The experimental correlation functions are also compared to model predictions from different models. Finally, three-dimensional unlike-sign correlation functions are presented.

## 4.1 Like-sign kaon correlation function

The measured raw like-sign kaon correlation functions were corrected for misidentification of particle and momentum resolution. While the purity correction was applied according to Eq. 3.5, the effect of the momentum resolution was restored via Eq. 3.15. Then the one-dimensional corrected correlation functions were fitted by Eq. 3.6. Figure 4.1 shows example of one-dimensional correlation function for $0.35 < k_T < 0.65$ GeV/$c$ and centrality 10-30%. The left panel of Figure 4.1 presents the corrected correlation function for positively charged kaons and the correlation function constructed for the negatively charged kaons is shown in the right panel of Figure 4.1. The lines represents the best fits to the data by using Eq. 3.6. As can be seen, in all cases the fits well describe the experimentally measured and corrected correlation functions.

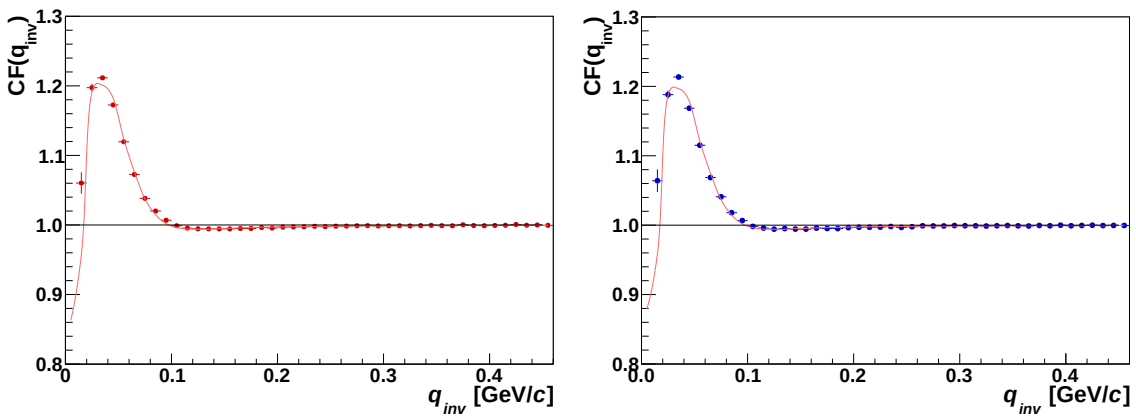


**Figure 4.1:** One dimensional like-sign correlation function for positive (left) and negative (right) kaons for centrality 10-30% and $0.35 < k_T < 0.65$ GeV/c. The lines represent the best fit to the data by using Eq. 3.6.

Results from fits of correlation function for different centralities and $k_T$ bins are presented in Figure 4.2. Here the $\lambda$ parameter, source radius $R_{inv}$ and the normalization factor $\mathcal{N}$ are shown as a function of the centrality and pair transverse momentum $k_T$.

As can be seen the source radii $R_{inv}$ increase with the centrality. The falling of the $R_{inv}$ with the pair transverse momentum $k_T$ qualitatively agrees with the effects expected from a system undergoing a transverse expansion where pairs with the larger transverse momentum are emitted from a smaller effective source than the pairs with the smaller $k_T$, as it was already discussed in the Chapter 3. The behavior of the $\lambda$ parameter is not monotonic. In most cases the $\lambda$ parameter slightly increases for two lower $k_T$ bins and then decreases.

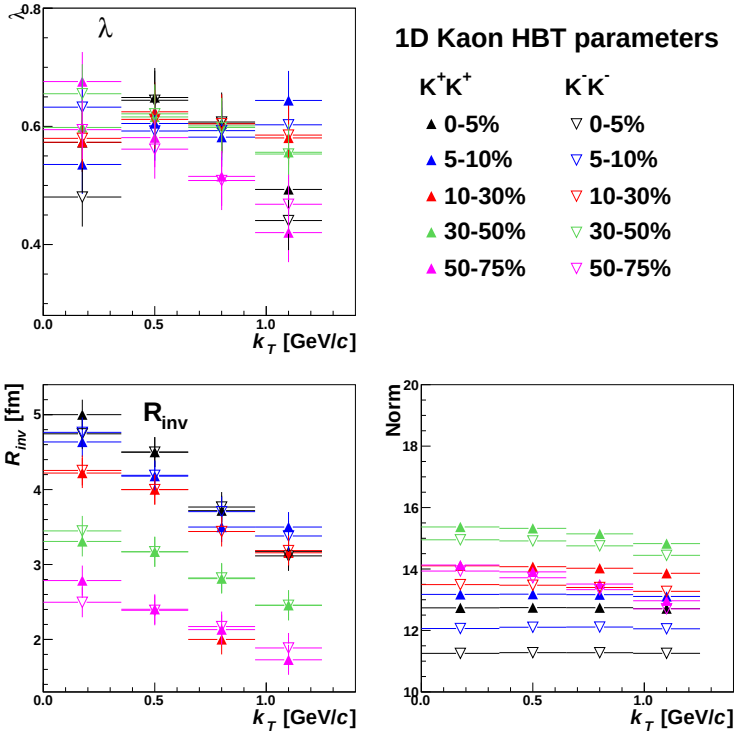


**Figure 4.2:** Fit results: $\lambda$ parameters, source radii $R_{inv}$ and normalization factors $\mathcal{N}$ as a function of $k_T$ and centrality.

The errors of the fit results are dominated by systematic uncertainties which were estimated by varying the fit ranges. Within presented errors, no significant difference between source radii $R_{inv}$ from positive and negative kaons is observed.

More information about the kaon source can be obtained from a three-dimensional correlation function. Similar procedure as for the one-dimensional correlation functions was used for correction of the three-dimensional correlation functions on misidentification of particle and momentum resolution. The fitting was performed by the parametrization given in Eq. 3.7. An example of fitted three-dimensional correlation function for centrality 10-30% and $0.35 < k_T < 0.65$ GeV/$c$ is shown in Figure 4.3.

Figure 4.4 shows the HBT parameters $\lambda$, $R_{out}$, $R_{side}$ and $R_{long}$ for four centralities as a function of the pair transverse momentum $k_T$, separately for positively and negatively charged kaons. The extracted HBT radii decrease as a function of $k_T$. While the observed decrease of the $R_o$ and $R_l$ is produced by the transverse flow, the falling of $R_l$ radii is ascribed to the longitudinal expansion of the source. The $\lambda$ parameter slightly increases with $k_T$. For most measured values there is a good agreement between the parameters extracted from the positively and negatively charged kaons. The first and the last $k_T$ bin for centrality 50-75% is statistically limited, therefore the fits for these bins are unstable. Recently, the femtoscopy with the like-sign kaon in Au+Au collisions at energy $\sqrt{s_{\rm NN}} = 200$ GeV was also performed by the PHENIX experiment [29]. Figure 4.5 shows the comparison of the

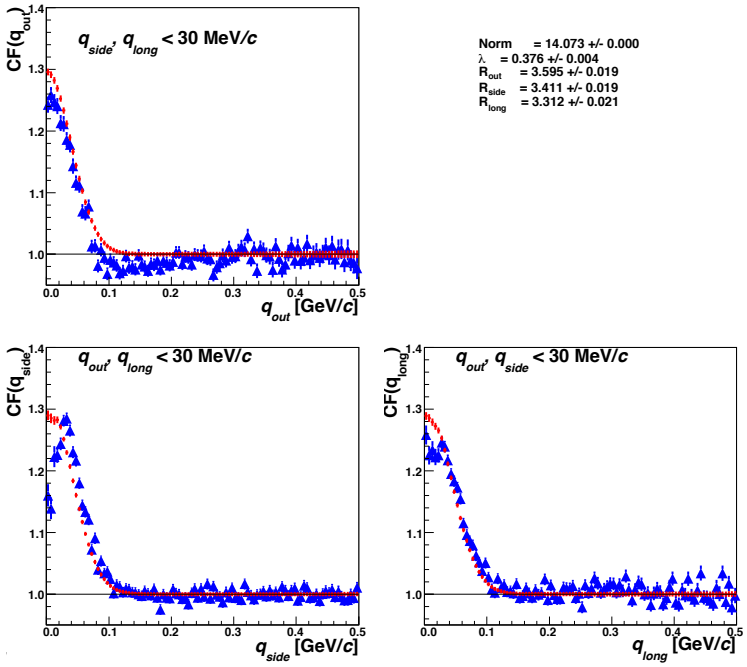


**Figure 4.3:** Projection of the three-dimensional correlation function and corresponding fits according Eq. 3.7 for positive kaons for centrality 10-30% and $0.35 < k_T < 0.65$ GeV/$c$.

extracted HBT radii by the PHENIX collaboration for the 0-10% most central events with those obtained in this analysis at the same beam energy, collision system and centrality. In general, the same trend of the HBT radii is observed, however our results are slightly lower. The presented results contains only the statistic errors.

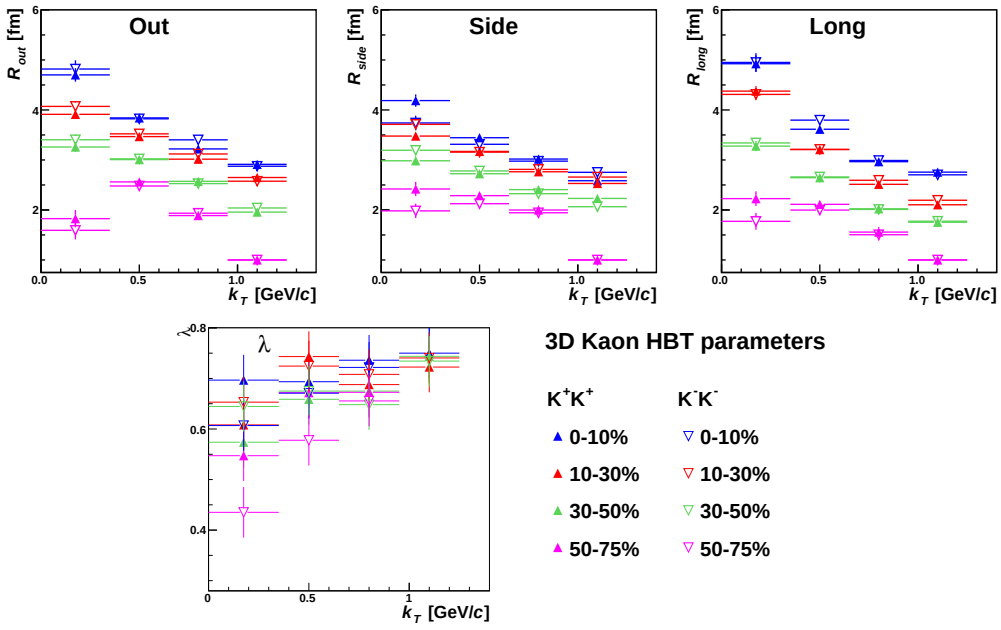


**Figure 4.4:** Fit results: $\lambda$ parameter, HBT radii $R_{out}$, $R_{side}$ and $R_{long}$ as a function of $k_T$ and centrality.

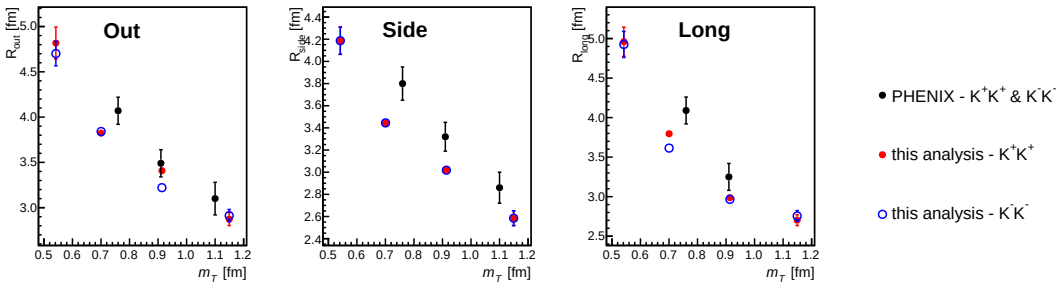


**Figure 4.5:** Comparison of extracted HBT radii $R_{out}$, $R_{side}$ and $R_{long}$ from Au+Au collision at $\sqrt{s_{\rm NN}}$ = 200 GeV to PHENIX results [29] for the same beam energy, collision system and centrality.

### 4.1.1 Blast-wave parametrization

It was already discussed that in order to obtain complete space-time extents of the source it is necessary to employ a model describing four-dimensional particle emission. One of the most standard tools in femtoscopy for such a purpose is the blast-wave parametrization [12] (see Chapter 1) which is designed to describe the freeze-out configuration with minimal set of parameters. The same blast-wave model which was described in detail in Chapter 3 is also used in this section. The extracted space-time extent by the blast-wave parametrization will be used in the next section for the parametrization of the source in more sophisticated hydrodynamical models and theoretical calculations.

Since the significant difference between the extracted HBT radii from the measured pairs of positive and negative kaons was not observed, it was possible to combine the measured pairs of kaons to decrease statistics uncertainties. Then the blast-wave parametrization was used for fitting the obtained kaon HBT radii and the particle spectra with a single set of free parameters. The combined particle spectra of pions, kaons and protons were simultaneously used in the fit to constrain the temperature and the flow velocity. Here, the data on $p_T$ spectra are taken from [30]. Contrary to the most general case when the blast-wave model employs eight independent parameters to describe the studied system, in this analysis due to the unavailability of the event plane only five parameters were used: the freeze-out temperature $T$, the maximum transverse rapidity $\rho_0$, the radius of the source $R$, the system proper time $\tau$ and the emission duration $\Delta\tau$. The combined kaon HBT radii with the blast-wave fits are presented in Figure 4.6. As can be seen the blast-wave parametrization is able to successfully describe the measured HBT radii, however some deviations are observed for the lowest centrality 50-75%.

| Centrality[%] | $T$ [MeV] | $\rho_0$ | $R$[fm] | $\tau$[fm/$c$] | $\Delta\tau$ [fm/$c$] |
|---|---|---|---|---|---|
| 0-10 | 104±3 | 1.02±0.01 | 11.1±0.3 | 6.8±0.3 | 2.8±0.1 |
| 10-30 | 106±3 | 1.00±0.02 | 8.8±0.2 | 4.9±0.3 | 2.8±0.2 |
| 30-50 | 111±6 | 0.91±0.05 | 7.5±0.3 | 4.4±0.3 | 1.6±0.1 |
| 50-75 | 115±10 | 0.89±0.08 | 3.4±0.3 | 3.0±0.2 | 0.7±0.1 |

**Table 4.1:** Extracted parameters from a blast-wave fit to kaon HBT radii and pion, kaon and proton transverse momentum spectra at $\sqrt{s_{\rm NN}}$ = 200 GeV.

The extracted parameters from the blast-wave model are shown in Table 4.6 for four centrality. Most of the parameters and their dependence on the collisions centrality agree with the expectations. While the temperature $T$ decreases with the increasing centrality, the maximum transverse rapidity $\rho_0$ increases with increasing centrality. Such behavior of these parameters reflects increasing source size with the centrality. The expansion of the larger system takes longer time as shown by the decreasing system evolution time $\tau$ and the emission duration $\Delta\tau$ with the decreasing the centrality.

It is especially interesting to compare our extracted blast-wave parameters with the parameters from pion femtoscopy [31]. Figure 4.7 presents the comparison of the obtained blast-wave parameters from this work and from the STAR analysis of pion femtoscopy [31]. The results are also compared to PHENIX results on blast-wave fit of the kaon HBT radii [29].

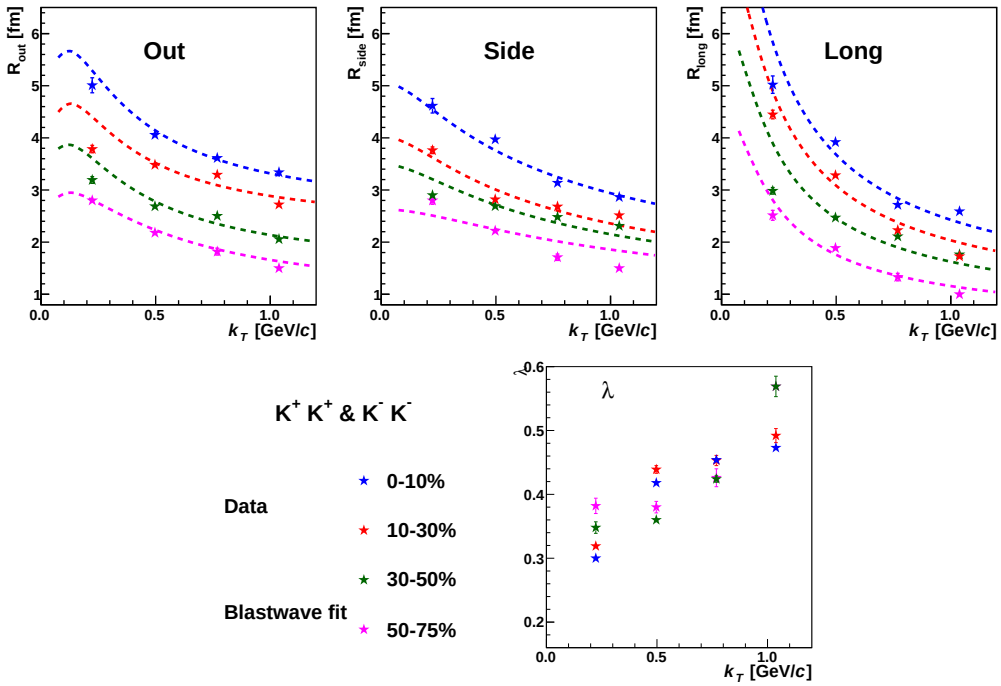


**Figure 4.6:** Comparison of extracted kaon HBT radii $R_{out}$, $R_{side}$ and $R_{long}$ with the blast-wave fit represent by colored lines for four centrality and four $k_T$ bins.

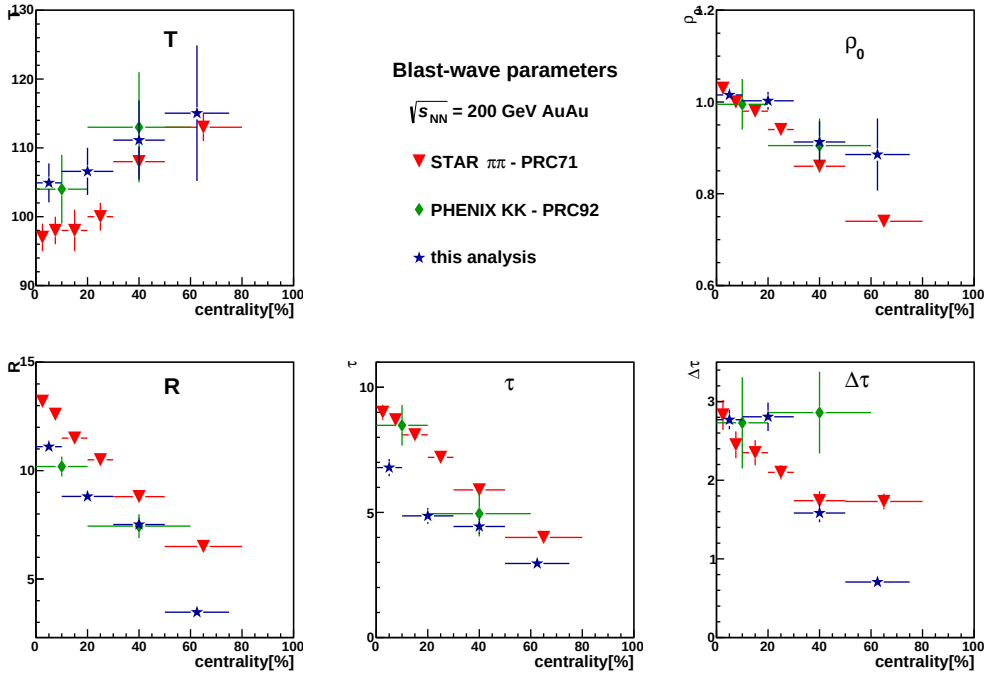


**Figure 4.7:** Comparison of extracted blast-wave parmeters from fits to HBT radii. The red stars represents results from fit $\pi - \pi$ HBT radii, the green diamond is for PHENIX results on $KK$ femtoscopy and the blue stars represents blast-wave parameters obtained in this analysis.

As can be seen the blast-wave parameters from kaon femtoscopy seem to slightly differ from those parameters obtained from the STAR pion HBT radii [31]. For given centrality, the temperature $T$ of the system obtained in our analysis is higher than for pion femtoscopy. The measured radius $R$ of the source, system evolution time $\tau$ and emission duration $\Delta\tau$ are also smaller than those obtained from the previous pion femtoscopy [31]. All of these observed differences would suggest that the kaons could be emitted earlier than pions due to their relative smaller cross section [32] with hadronic matter in comparison with pions. However one has to be very careful, because this conclusions need to be further tested and especially systematic errors have to be carefully evaluated.

## 4.2 Unlike-sign kaon correlation function

In this section experimental correlation function for unlike-sign kaon is studied in detail. The measured raw functions were corrected for misidentification of particle in a same ways as like-sign kaon correlation functions via Eq. 3.5. The correction for the momentum resolution has not been applied so far. In the future when the unlike-sign kaon correlation function is fitted, the momentum resolution will be useful for fitting in the region of the low $q_{inv}$. The corrected unlike-sign kaon correlation functions for centrality 0-5% and centrality 30-50% for 4 $k_T$ bins are shown in Figure 4.8 and Figure 4.9.

### 4.2.1 Comparison of unlike-sign one-dimensional correlation to Lednický model

The experimental results of the unlike-sign one-dimensional correlation function are compared to the theoretical prediction from Lednický model [14] in Figure 4.8 and Figure 4.9. The theoretical functions were calculated accord to Eq.1.1. Similarly, in the case of the one-dimensional correlation functions, the source was characterized by one-dimensional Gaussian in the PRF with a parameter $R_{inv}$. Here the individual $R_{inv}$ are those extracted from fitting like-sign kaon correlation function (see Figure 4.2). The Lednický FSI model [14] includes the treatment of $\phi(1020)$ resonance in the final state. The extended femtoscopics formalism, which contains generalized form of the smoothness approximation, is included in this model. As authors of the models claim, the generalized smoothness assumption is needed for correct description of the correlation function in the region of the resonance. Since the theoretical function does not include effects contained in the experimental $\lambda$ parameter, it is scaled for correct comparison according to

$$CF = \left(CF^{theo} - 1\right)\lambda + 1, \tag{4.1}$$

where $\lambda$ parameter was obtained from the fit to the like-sign kaon correlation function (see Figure 4.2).

Example of comparison of unlike-sign kaon correlation function to model calculations is shown in Figure 4.8 and Figure 4.9. The measured unlike-sign kaon correlation functions for the most central collisions and for 4 $k_T$ bins are shown in Figure 4.8. Figure 4.9 presents the comparison of the theoretical function to experimentally measured functions for mid-peripheral collisions, centrality 30 - 50%.

As can be seen, the model reproduces well the overall structure of the measured correlation functions. At the region of the low $q_{inv}$ where the well-known attractive Coulomb interaction and the strong interaction in s-wave are present, the model is able to describe the strength of the correlation. For most central collisions and low $k_T$ mid-peripheral, the Lednický model is also able to predict the measured correlation function in the region of the resonance region.

However, with decreasing source size (decreasing centrality and higher $k_T$) the model starts to underestimate the strength of the correlation function. Even when the correlation function is underestimated by Lednický model in the region of the resonance, the model still describes the correlation at the low $q_{inv}$. The small difference in the low $q_{inv}$ can be ascribed to effect of the smearing and/or possibly residual correlations.

It was predicted by Lednický [14], that the strength of the correlation should change with the source size $R_{inv}$ as $R_{inv}^{-3}$ The right panel of Figure 4.10 shows the height of the peak of the resonance as a function of the measured like-sign source size $R_{inv}$.

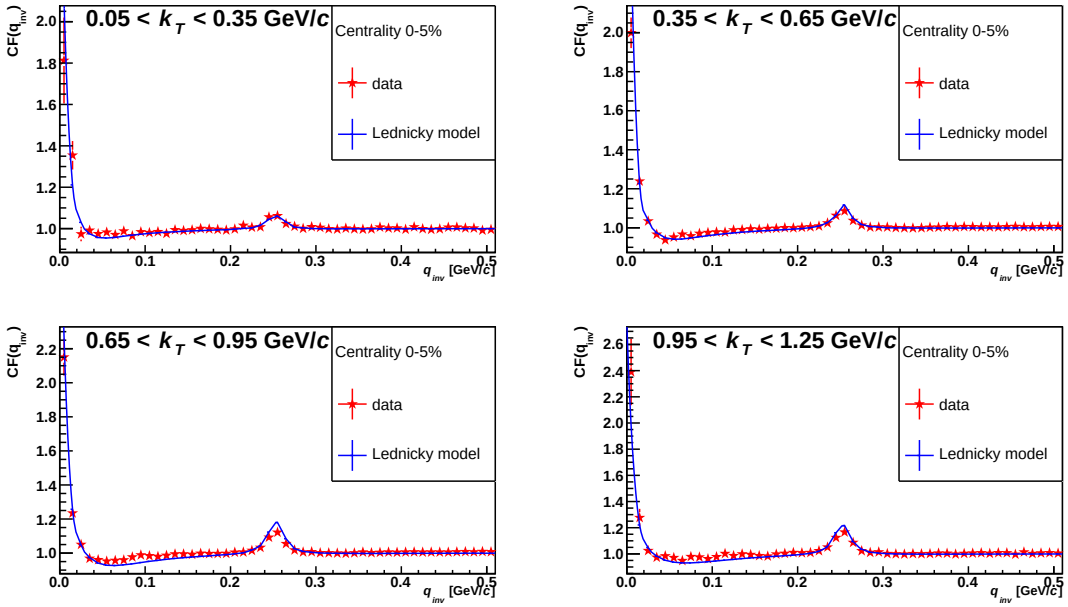


**Figure 4.8:** Comparison of experimental unlike-sign kaon correlation function to theoretical calculation for centrality 0-5% centrality for 4 different $k_T$ bins.

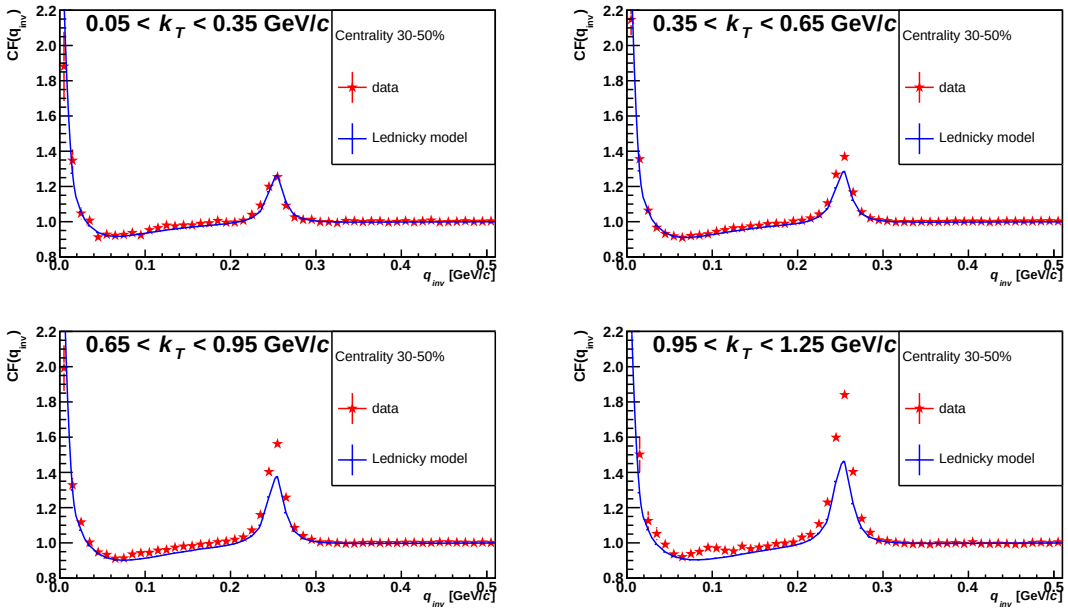


**Figure 4.9:** Comparison of experimental unlike-sign kaon correlation function to theoretical calculation for centrality 30-50% centrality for 4 different $k_T$ bins.

The dependence of the height of the peak on the $R_{inv}^{-3}$ is shown in the left panel of Figure 4.10. As can be seen, the peak height scales with source size as $R_{inv}^{-3}$. In particular, it is especially interesting to note that the same source sizes $R_{inv}$ were obtained from different correlation functions. The $R_{inv}$ is the same for higher centrality and higher $k_T$ as well as for lower centrality and lower $k_T$. Within errors arising from the extraction of the source radii by fitting like-sign kaon correlation function, the height of the peaks are consistent. It indicates that the correlation function in the region of the

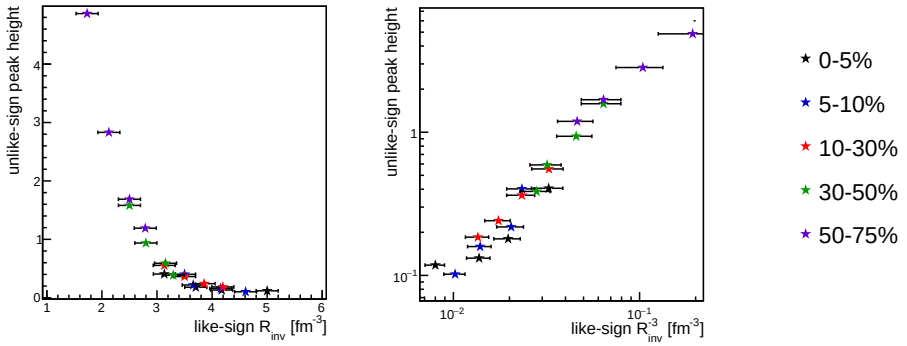


**Figure 4.10:** Left: The dependence of the height of the peak as a function of measured source radii $R_{inv}$ from like-sign kaon correlation function. Right: The dependence of the height of the peak as a function of inverse volume of the system $\sim R_{inv}^{-3}$, where the source size $R_{inv}$ is obtained from one-dimensional like-sign correlation functions.

resonance is indeed connected to the source size and does not depend for example on temperature.

In the following subsection the experimental correlation functions are compared to hydrodynamic model predictions, namely to THERMINATOR 2. Such a model comparison can bring additional insight into the interpretation of the results.

### 4.2.2 Comparison of unlike-sign one-dimensional correlation with THERMINATOR 2

The experimentally constructed unlike-sign kaon correlation functions were also compared with prediction by THERMINATOR 2 [11]. It is thermal heavy-ion generator dedicated to studies of the statistical production of particles in ultra-relativistic heavy-ion collisions [11]. THERMINATOR 2 includes various shape of the freeze-out hypersurface and the expansion velocity field, including 2+1 as well as 3+1 dimensional profiles. Behind the statistical approach, it contains hadronic resonances which significantly contribute to the observables.

The freeze-out configuration of the source emitting particles was characterized by Blast-wave model with following set of parameters: temperature $T$, barion chemical potential $\mu_B$, strangeness potential $\mu_s$, third component of isospin $\mu_I$, transverse velocity $v_T$, maximal transverse radius $\rho_{max}$ and the proper time at freeze-out $\tau$. As can be seen, it is quite different blast-wave model than the one which was used for fitting kaon HBT radii was discussed in the previous section. Compared to the Gaussian parametrization of the source, the blast-wave parametrization is more realistic and inherently introduces $k_T$ dependence of radii as well as $r - k$ correlations [14]. The relative distance of emission point of two particles is correlated with relative pair momentum. Such phenomena should reflect in the height of the peak.

In the presented analysis, the setup [33] for collision energy $\sqrt{s_{\rm NN}}$=200 GeV was used. The interaction between particles was calculated by the already discussed Lednický model [14]. Figure 4.11 shows the comparison of experimental unlike-sign correlation function for the most central collisions with calculations where the source was parametrized by the Gaussian as well as blast-wave parametrization from THERMINATOR 2. As can be seen, both of the used source parameterizations successfully reproduces the shape of the correlations and describe the strength of correlations in the region of the resonance.

However, the blast-wave parametrization used in THERMINATOR model is different from the previously employed and includes natively $\lambda$ parameter, this comparison provide the first look on case when the theoretical calculation is performed with more realistic source parametrization. In future the similar calculations will be done with same blast-wave model, which was used for fitting. It enables to compare experimental correlation function for other centralities.

In the future model like HYDJET++ or THERMINATOR 2 can be used for estimation of the effect of residual correlations. These effect arise from the presence of particles which come from weak

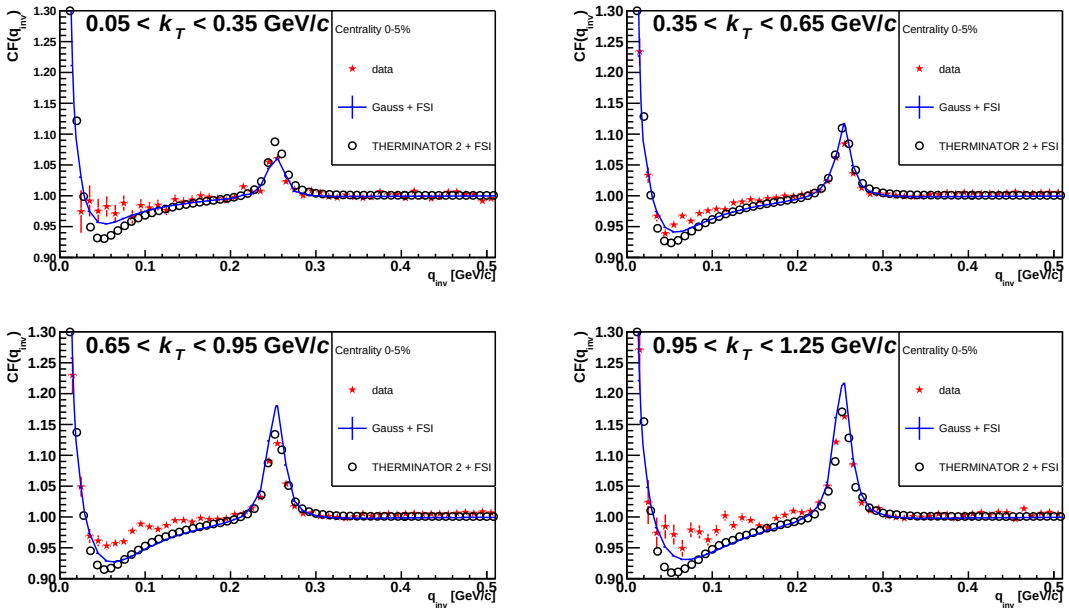


**Figure 4.11:** Comparison of experimental unlike-sign kaon correlation function to two model calculations for centrality 0-5% and 4 different $k_T$ bins. The blue lines represent the case when the source is parametrized by the Gaussian. The open blue circle shows correlation function calculated f by THERMINATOR 2.

decays of already correlated particles. THERMINATOR has been specially develop for such studies and has been commonly employed by experiment at RHIC [34], [35] and LHC[36]. Figure 4.12 shows contribution of two resonance decays to kaon transverse momentum.

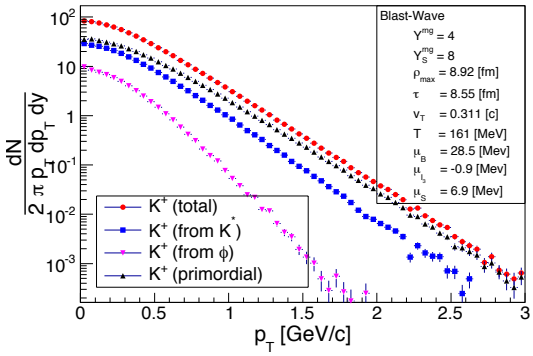


**Figure 4.12:** The transverse momentum spectra of positive kaon with two resonance decay contribution.

# Conclusions and Outlook

The main purpose of the analysis introduced in this work is a femtoscopic study of two-particle correlation function in a system where narrow near-threshold resonance is present. The correlation function is predicted to be highly sensitive to the source size and momentum-space correlations in the region of the resonance. System of unlike-sign kaons is ideally suited for such a study since it contains the $\phi(1020)$ resonance. The presented analysis was performed on minimum bias data from Au+Au collisions at $\sqrt{s_{\rm NN}}$ =200 GeV collected by the STAR experiment. It is the first high-statistics systematic study of unlike-sign kaon correlation function in heavy-ion collisions.

The available statistics and selection criteria allowed to construct one dimensional correlation functions for pairs of unlike-sign kaons for five collision centralities and four different $k_T$ bins. First results for $k_T$-integrated three dimensional correlation functions were also obtained. All measured unlike-sign kaon correlation functions (Figure 2.11) exhibit strong centrality and transverse pair momentum dependence in the region of the $\phi$ resonance.

In order to compare the experimentally measured correlation functions with theoretical predictions and model calculations a femtoscopic analysis with like-sign kaons was performed using the same centrality classes and $k_T$ bins. The extracted space-time extents were then used for parameterizing the source in the theoretical calculations of the unlike-sign kaon correlation functions. This like-sign analysis uses the highest available dataset and is hence the most precise measurement of kaon HBT radii at RHIC. The preliminary results on the HBT radii ($R_{out}, R_{side}, R_{long}$) obtained from three dimensional correlation functions (4.4) follow characteristic trends in the centrality and $k_T$ confirming the presence of the collective expansion of the system. The comparison with recently published PHENIX results (4.5) shows small systematic difference towards smaller values. The measured radii and kaon spectra were fitted by blast-wave model obtaining parameters which describe the kaon source at the kinetic freeze-out. The larger available statistics at STAR has resulted in a larger number of $k_T$ bins for each centrality and allowed better constraints of the blast-wave fits. The extracted blast-wave parameters and their dependence on collision centrality agree with the expectations, following similar trends as for pions. The comparison with STAR pion blast-wave results (Figure 4.7) reveals systematically smaller size, higher temperature and smaller transverse velocity. This may indicate possible earlier emission of kaon from the system. However, this conclusions need to be further tested and especially systematic errors have to be carefully evaluated.

After the extraction of source parameters from like-sign correlation function, the experimental unlike-sign correlation functions were compared to theoretical calculations based on the improved Lednický model of the final-state interaction. This model includes the treatment of $\phi(1020)$ resonance due to final-state interaction and therefore it should be able to reproduce the structure of the measured correlations. The results were compared to calculations using simple Gaussian parameterization of the kaon source as well hydro-based models: THERMINATOR 2. All calculations qualitatively reproduce the measured correlation function, however their quantitative agreement gets worse for smaller systems. Although the Lednický model contains the generalized smoothness assumption, the observed underestimation of the strength of the correlation in the region of the resonance for lower centralities and higher $k_T$ bins can be probably ascribed to a breakdown of the smoothness approximation - one of the basic assumption in femtoscopy. Other explanation, supported by the author of the model, is an interplay between thermally produced resonances and those produced as a result of the final state interaction. If the thermal production and the production via final-state interaction are not equivalent, the free room which the FSI model leaves should be filled by the thermal production of the $\phi(1020)$ resonance. In such a case, the Lednický model does not properly describe the correlation function in the resonance region for the most central collisions. Currently there is no clear consensus on the side of the theory, hence the high-statistics results presented in this thesis can help to clarify the issue.

The results in this thesis are first systematic study of two-particle correlation function in a system where narrow near-threshold resonance using the femtoscopic formalism. For this reason there is still much work that can be done in the future. To strengthen the conclusions detailed study of systematic errors is under way. Also since radii extraction is at this point dominated by systematic uncertainties

it may be possible to increase the number of $k_T$ bins.

One of the most interesting challenges is related to the comparison of the measured correlation functions with the theoretical calculations and hydrodynamics models. The correct description of experimental unlike-sign kaon correlation function may need better parametrization of the freeze-out configuration of the source emitting particle in combination with detailed theoretical study of femtoscopic formalism in the region of resonace. In future, such analysis can provide additional insight into the studied system via femtoscopic measurements and bring complementary information to the standard measurements at very low relative momentum.

## BIBLIOGRAPHY


[1] Gerson Goldhaber". Influence of bose-einstein statistics on the antiproton-proton annihilation process. *Physical Review*, 120(1):300–312, 1960.

[2] G. I. Kopylov. Like particle correlations as a tool to study the multiple production mechanism. *Phys. Lett.*, B50:472–474, 1974.

[3] Mercedes Lopez Noriega. *Pion Interferometry in AuAu Collisions at a Center of Mass Energy per Nucleon of 200 GeV*. PhD thesis, The Ohio State University, 2004.

[4] L. Adamczyk et al. Beam-energy-dependent two-pion interferometry and the freeze-out eccentricity of pions measured in heavy ion collisions at the STAR detector. *Phys. Rev.*, C92(1):014904, 2015.

[5] L. Adamczyk et al. Freeze-out dynamics via charged kaon femtoscopy in sqrt(sNN) = 200 GeV central Au + Au collisions. *Phys. Rev.*, C88:034906, 02 2013.

[6] L. Adamczyk et al. Measurement of Interaction between Antiprotons. *Nature*, 527:345–348, 2015.

[7] Michael Annan Lisa, Scott Pratt, Ron Soltz, and Urs Wiedemann. Femtoscopy in relativistic heavy ion collisions. *Ann.Rev.Nucl.Part.Sci.*, 55:357–402, 2005.

[8] Ulrich W. Heinz. How to extract physics from HBT radius parameters. *Nucl.Phys.*, A610:264C–277C, 1996.

[9] Y.F. Wu, Ulrich W. Heinz, B. Tomasik, and U.A. Wiedemann. Yano-Koonin-Podgoretskii parametrization of the HBT correlator: A Numerical study. *Eur.Phys.J.*, C1:599–617, 1998.

[10] I.P. Lokhtin, L.V. Malinina, S.V. Petrushanko, A.M. Snigirev, I. Arsene, et al. Heavy ion event generator HYDJET++ (HYDrodynamics plus JETs). *Comput.Phys.Commun.*, 180:779–799, 2009.

[11] Mikolaj Chojnacki, Adam Kisiel, Wojciech Florkowski, and Wojciech Broniowski. THERMINATOR 2: THERMal heavy IoN generATOR 2. *Comput. Phys. Commun.*, 183:746–773, 2012.

[12] Fabrice Retiere and Michael Annan Lisa. Observable implications of geometrical and dynamical aspects of freeze out in heavy ion collisions. *Phys.Rev.*, C70:044907, 2004.

[13] Michael Annan Lisa and Scott Pratt. Femtoscopically Probing the Freeze-out Configuration in Heavy Ion Collisions. 2008.

[14] R. Lednicky. Femtoscopic correlations and final state resonance formation. *Phys. Part. Nucl. Lett.*, 8:965–968, 2011.

[15] J. Pochodzalla et al. Two-particle correlations at small relative momenta for $^{40}$induced reactions on $^{197}$Au at $E/A$ =60 mev. *Phys. Rev. C*, 35:1695–1719, May 1987.

[16] Mike Lisa. Femtoscopy and hadrochemistry. In *9th Workshop on Particle Correlations and Femtoscopy*, 2013.

[17] Byron K. Jennings, David H. Boal, and Julian C. Shillcock. Two-particle correlation functions in the thermal model and nuclear interferometry descriptions. *Phys. Rev.*, C33:1303–1306, 1986.

[18] S. V. Afanasiev et al. Bose–Einstein correlations of charged kaons in central Pb+Pb collisions at $E_{beam}$ =158 GeV per nucleon. *Phys. Lett.*, B557:157–166, 2003.

[19] Petr Chaloupka. Femtoscopy with multi-strange baryons at RHIC. *Phys.Part.Nucl.Lett.*, 8:973–976, 2011.

[20] P. Chaloupka, M. Sumbera, and L.V. Malinina. pi Xi correlations: Model comparison and Xi*(1530) puzzle. *Acta Phys.Polon.*, B40:1185–1192, 2009.

[21] Z. Chajecki, T.D. Gutierrez, M.A. Lisa, and M. Lopez-Noriega. AA versus PP (and dA): A Puzzling scaling in NBT and RHIC. 2005.

[22] H. Bichsel. A method to improve tracking and particle identification in TPCs and silicon detectors. *Nucl.Instrum.Meth.*, A562:154–197, 2006.

[23] Christopher Daniel Anson. *Energy dependet Hanbury Brown - Twiss interferometry and the freeze-out eccentricity of heavy ion collisions at STAR*. PhD thesis, The Ohio State University, 2014.

[24] Adam Kisiel, editor. *CorrFit: a program to fit arbitrary two-particle correlation functions*, volume 49(Supplement 2). Nukleonika, 2004.

[25] M. G. Bowler. Coulomb corrections to Bose-Einstein correlations have been greatly exaggerated. *Phys. Lett.*, B270:69–74, 1991.

[26] L. Ahle et al. System, centrality, and transverse mass dependence of two-pion correlation radii in heavy ion collisions at 11.6$a$ and 14.6$a$GeV/$c$. *Phys. Rev. C*, 66:054906, Nov 2002.

[27] Petr Chaloupka. *Femtoscopy with multi-strange baryons at RHIC*. PhD thesis, Charles University in Prague, 2010.

[28] Hanna Zbroszczyk. *Studies of Baryon-Baryon Correlations in Relativistic Nuclear Collisions Registered at the STAR Experiment*. PhD thesis, Warsaw University of Technology, 2008.

[29] A. Adare et al. Systematic study of charged-pion and kaon femtoscopy in Au + Au collisions at $\sqrt{s_{NN}}$=200 GeV. *Phys. Rev.*, C92(3):034914, 2015.

[30] S. S. Adler et al. Identified charged particle spectra and yields in Au+Au collisions at S(NN)**1/2 = 200-GeV. *Phys. Rev.*, C69:034909, 2004.

[31] J. Adams et al. Pion interferometry in Au+Au collisions at S(NN)**(1/2) = 200-GeV. *Phys.Rev.*, C71:044906, 2005.

[32] J. Beringer et al. Review of particle physics*. *Phys. Rev. D*, 86:010001, Jul 2012.

[33] Hanna Zbroszczyk. Two-particle correlations using therminator model for bes program. presentation on ICNFP 2015.

[34] L. Adamczyk et al. $\Lambda\Lambda$ Correlation Function in Au+Au collisions at $\sqrt{s_{NN}}$ = 200 GeV. *Phys. Rev. Lett.*, 114(2):022301, 2015.

[35] Fu-Quiang Wang. Residual correlation in two proton interferometry from Lambda proton strong interactions. *Phys.Rev.*, C60:067901, 1999.

[36] Jaroslav Adam et al. One-dimensional pion, kaon, and proton femtoscopy in Pb-Pb collisions at $\sqrt{s_{\rm NN}}$ =2.76 TeV. *Phys. Rev.*, C92(5):054908, 2015.